

pubs.acs.org/JPCC Article

# Nanomolecular Metallurgy: Transformation from Au<sub>144</sub>(SCH<sub>2</sub>CH<sub>2</sub>Ph)<sub>60</sub> to Au<sub>279</sub>(SPh-*t*Bu)<sub>84</sub>

Kalpani Hirunika Wijesinghe, Naga Arjun Sakthivel, Luca Sementa, Bokwon Yoon, Alessandro Fortunelli,\* Uzi Landman,\* and Amala Dass\*



**Cite This:** *J. Phys. Chem. C* 2021, 125, 20488–20502



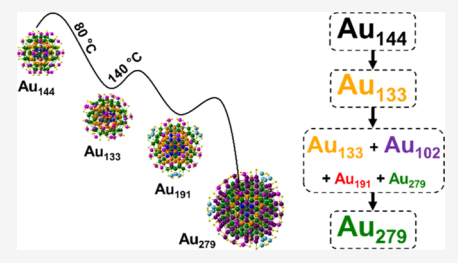
**ACCESS** 

Metrics & More



si Supporting Information

ABSTRACT: Transformation brought about by ligand exchange is one of the effective methods for the synthesis of gold-thiolate nanomolecules (AuNMs). In this method, the AuNMs are treated with an excess exogenous thiol at an elevated temperature. It has been found that the ligand exchange is often accompanied by conversion of the metal core from a larger size to a smaller size, depending on the type of exogenous capping ligand employed. In this work, we present the transformation of a smaller-size AuNM (133 Au atoms) to a larger-size AuNM (279 Au atoms). Here, we observe that the Au<sub>144</sub>(SCH<sub>2</sub>CH<sub>2</sub>Ph)<sub>60</sub> AuNM in the presence of 4-tert-butylbenzenethiol under refluxing conditions first transforms to Au<sub>133</sub>(SPh-tBu)<sub>52</sub>, and then with the



transformation reaction proceeding to form larger-sized AuNMs, Au<sub>191</sub>(SPh-tBu)<sub>66</sub> and Au<sub>279</sub>(SPh-tBu)<sub>84</sub>. The reaction progress was monitored with matrix-assisted laser desorption ionization mass spectrometry (MALDI-MS) and UV-vis spectroscopy, and the intermediates and AuNMs were identified with electrospray ionization (ESI) MS. In conjunction with the above experiments, theoretical explorations using density functional theory calculations have been carried out, probing the energetics and thermodynamic stabilities underlying the observed size-changing transformations. It also elucidates the systematic size-dependent trends in the electronic structure of the original 144-gold-atoms-capped AuNM and the transformation products, including analysis of formation of superatom shells through the use of the core-cluster-shell model.

## **■ INTRODUCTION**

Gold-thiolate nanomolecules (AuNMs) having a precise number of Au metal atoms protected by thiolate ligands have been gaining significant attention in biosensing, catalysis, energy devices, supramolecular chemistry, and as therapeutic agents. These AuNMs have been studied extensively and were characterized by electrospray ionization mass spectrometry (ESI-MS), matrix-assisted laser desorption ionization time-of-flight mass spectrometry (MALDI-TOF-MS), single-crystal X-ray diffraction (sc-XRD), and UV-visible spectroscopy. AuNMs have been found to exhibit unique chemical, physical, and optical properties, governed by their size and the thiolate ligand protecting the metal core.

The main structural components of the AuNMs are: (i) the inner core, made solely of mutually interacting Au atoms, which do not bond directly to the capping ligand molecules, and core surface Au atoms, which interact with the capping ligands; (ii) Au-SR staples, which can be monomeric (SR-Au-SR), dimeric (SR-Au-SR-Au-SR), or trimeric (SR-Au-SR-Au-SR-Au-SR), etc.; and (iii) the thiolate capping surface. The capping ligands (thiolates in this study) contribute to the structure, stability, electrochemical, and physicochemical properties of the AuNMs. Thiolate ligands commonly used in the synthesis of AuNMs can be classified into three groups, namely aliphatic-like (e.g., *n*-butane thiol, phenylethane thiol), aromatic (e.g., thiophenol, 4-tert-butylbenzene-

thiol), and bulky (e.g., tertiary butyl thiol, 1-adamantane thiol). Furthermore, a desired, most stable AuNM composition can be achieved by altering the thiol class being employed, the reaction temperature, the concentration of the reactants, and the synthesis method.  $^{15-19,25-27}$ 

Among the various methods used for the synthesis of AuNMs, ligand exchange is one of the most widely used ones. The AuNMs prepared through the use of a chosen capping thiol ligand are subsequently treated with an exogenous thiol ligand at an elevated temperature. <sup>26,30–32</sup> When the exogenous ligand was reacted with the AuNM, the thermodynamically stable structure corresponding to the existing thiolate ligand gets disrupted. The AuNM reaches a new thermodynamically stable structure upon heating with an exogenous thiol. This transformation occurs with the loss or gain of Au atoms in the course of the ligand exchange process. <sup>30,31,33</sup> The number of ligands may or may not change in the course of conversion.

In 2016, a study was published describing an exchange process where the size of the AuNM, i.e., the number of Au

Received: May 12, 2021
Revised: August 12, 2021
Published: September 8, 2021





and thiol, was not changed, but with the difference in the ligand shell. At In that work,  $Au_{28}(SPh-tBu)_{20}$  was subjected to 80 °C in the presence of excess cyclohexanethiol (HS-c-C<sub>6</sub>H<sub>11</sub>), yielding ligand-exchanged  $Au_{28}(S-c-C_6H_{11})_{20}$ . Au<sub>28</sub>(SR)<sub>20</sub> (SR = SPh-tBu or S-c-C<sub>6</sub>H<sub>11</sub>) NMs have the same numbers of Au atoms and thiol ligands. When comparing the structures of the two AuNMs, it was found that they have the same core structure but different surface structures. In particular, both AuNMs have an  $Au_{20}$  core and eight bridging ligands. However,  $Au_{28}(c-C_6H_{11})_{20}$  has two monomeric and two trimeric staples, whereas  $Au_{28}(SPh-tBu)_{20}$  has four dimeric staples. This example illustrates that the structure of AuNMs may (and often does) depends on the capping ligand molecules.

A number of studies were reported describing ligand exchange processes where larger AuNMs transform to smaller AuNMs.  $^{30,31,36-38}$  The core size conversion of Au<sub>144</sub>(SCH<sub>2</sub>CH<sub>2</sub>Ph)<sub>60</sub> to Au<sub>133</sub>(SPh-tBu)<sub>52</sub> and Au<sub>99</sub>(SPh)<sub>42</sub> by thermochemical treatment in the presence of exogenous thiolate ligands has been reported. But no other core sizes were found in these studies.

The conversion of smaller AuNMs to larger AuNMs has been reported in a few studies.<sup>39-43</sup> When HSPh-tBu was allowed to react with Au<sub>30</sub>(S-tBu)<sub>18</sub> at 80 °C, it transformed to  $Au_{36}(SPh-tBu)_{24}$ . Interestingly, the reverse of the reaction also occurred, i.e., when Au<sub>36</sub>(SPh-tBu)<sub>24</sub> was subjected to thermochemical treatment with HS-tBu,  $Au_{36}(SPh-tBu)_{24}$  converted to  $Au_{30}(S-tBu)_{18}$ . Moreover, it has been successfully demonstrated that  $Au_{25}(SR)_{18}$  reacts with itself to form  $Au_{38}(SR)_{24}$  (SR =  $SC_3H_7$  and  $SC_4H_9$ ).<sup>40</sup> This fusion reaction was achieved by dissolving Au<sub>25</sub>(SR)<sub>18</sub> in toluene and subjected to 65 °C and no extra ligand or Au(I)-SR complex was added to the reaction mixture. The authors proposed that the size transformation reaction occurs by the formation of a precursor complex, where the initial driving force is the van der Waals interactions between the ligands of the two interacting clusters. 40 In another study, Au<sub>38</sub>(p-MBA)<sub>24</sub> and Au<sub>44</sub>(p-MBA)<sub>26</sub> were obtained from the seed-mediated growth of  $Au_{25}(p\text{-MBA})_{18}$ . The  $Au_{25}(p\text{-MBA})_{18}$  was reacted with [Au(I)-(p-MBA)] complex in the presence of CO to provide a mildly reductive environment where the solution's pH was maintained under basic condition, at room temperature.<sup>41</sup> It has been proposed<sup>41</sup> that a three-stage size hopping mechanism underlies the formation of  $Au_{44}(p-MBA)_{26}$ . First, the pregrowth step was performed where Au<sub>25</sub>(p-MBA)<sub>18</sub> is accumulated. This step is governed by kinetic factors. Subsequently, a size-growth step occurs, followed by a "sizefocusing" step, which depends on the adsorption of reductive species, CO; the latter step is governed by thermodynamic factors.

In the case of  $\mathrm{Au}_{23}(S\text{-}c\text{-}C_6H_{11})_{16}$  conversion to  $\mathrm{Au}_{28}(S\text{-}c\text{-}C_6H_{11})_{20}$ , the  $\mathrm{Au}_{23}(S\text{-}c\text{-}C_6H_{11})_{16}$  NM was oxidized in the presence of  $\mathrm{H}_2\mathrm{O}_2$  while no extra thiol or (Au-SR) polymer was added. The transformation of  $\mathrm{Au}_{25}(S\text{-}n\mathrm{Bu})_{18}$  to  $\mathrm{Au}_{28}(\mathrm{PPT})_{21}$  at room temperature in the presence of 2-phenylpropane-1-thiol (PPT) has been reported. In this case, it was proposed that the driving force of this process is the van der Waals interaction within the ligand shell and the bulkiness of the methyl group in the ligand.

We note that all of the aforementioned transformation chemistry studies were carried out for small AuNMs, leaving the area of size changes through transformation chemistry involving larger AuNMs unexplored. Motivated by the above, we report here joint experimental and theoretical investigations, demonstrating the conversion of Au<sub>144</sub>(SCH<sub>2</sub>CH<sub>2</sub>Ph)<sub>60</sub> to Au<sub>133</sub>(SPh-tBu)<sub>52</sub> in the presence of excess 4-tert-butylbenzenethiol ligand under refluxing conditions (~140 °C), where the reaction does not stop at Au<sub>133</sub>(SPh-tBu)<sub>52</sub> as observed previously,<sup>30</sup> but advances forward to form larger sizes, i.e., Au<sub>191</sub>(SPh-tBu)<sub>66</sub> and Au<sub>279</sub>(SPh-tBu)<sub>84</sub>. Briefly, pure Au<sub>144</sub>(SCH<sub>2</sub>CH<sub>2</sub>Ph)<sub>60</sub> was prepared according to the literature<sup>24</sup> and allowed to reflux with excess 4-tert-butylbenzenethiol. Small aliquots of samples were collected every 2 h and washed with methanol and water to remove excess thiol and impurities. The progress of the reaction was monitored with a UV-visible spectroscopy and MALDI-MS. ESI-MS was used to identify the molecular formula of the various AuNMs present in the samples.

Subsequent to the presentation of the experimental observations, we discuss the results of detailed theoretical explorations, using the density functional theory, probing the energetics and thermodynamic stabilities underlying the observed size-changing transformations. Furthermore, we carry out calculations and analyses that aim at elucidation of the electronic structures of the original 144-gold-atoms-capped AuNM and the sequence of transformation products  $[\mathrm{Au}_n(\mathrm{SPh}\text{-}t\mathrm{Bu})_m \ (n,m) = (133,52), \ (191,66)]$  including analysis of the formation of superatom shells through the use of the core-cluster-shell model. <sup>18,19</sup>

## **■ EXPERIMENTAL SECTION**

Materials. Tetrachloroauric(III) acid (HAuCl<sub>4</sub>·3H<sub>2</sub>O, Alfa Aesar, 99%), phenylethyl mercaptan (Sigma-Aldrich, 99%), 4-tert-butylbenzenethiol (TCI, 97%), tetraoctylammonium bromide (TOABr, Sigma-Aldrich, 98%), sodium tetrahydridoborate (NaBH<sub>4</sub>, Acros Organics, 99%), and trans-2-[3-(4-tert-butylphenyl)-2-methyl-2-propenylidene] malononitrile (DCTB matrix) (Fluka ≥99%). High-performance liquid chromatography (HPLC)-grade solvents tetrahydrofuran (THF), THF-butylated hydroxytoluene (THF-BHT), toluene, and methanol were used as received. Bio-Rad-SX1 beads (Bio-Rad) were used for size exclusion chromatography.

Instrumentation. UV—visible absorption spectra were collected using a Shimadzu UV-1601 instrument, and samples were dissolved in toluene. MALDI mass spectra were acquired using Voyager-De PRO MALDI-TOF-MS with the DCTB matrix. ESI mass spectra were obtained using Waters Synapt XS instrument, and the samples were mixed with a toluene—THF volume ratio of 1:9. For ease of ionization, cesium acetate was added to the sample. Baseline correction of the ESI spectra was done by polynomial correction (Figures 2, S2, S3, and S4).

Synthesis of  $Au_{144}(SCH_2CH_2Ph)_{60}$ . The synthesis of  $Au_{144}(SCH_2CH_2Ph)_{60}$  was done in two steps following the previous report. The first step is the synthesis of crude products, and the second step is the thermochemical treatment followed by size exclusion chromatography to get pure  $Au_{144}(SCH_2CH_2Ph)_{60}$ .

Crude Synthesis. HAuCl<sub>4</sub>·3H<sub>2</sub>O (0.177 g) was dissolved in 5 mL of distilled water. In a 250 mL round-bottom flask, 0.284 mg of TOABr was dissolved in 10 mL of toluene. Then, HAuCl<sub>4</sub> solution was added to the 250 mL round-bottom flask under 1200 rpm of stirring. HAuCl<sub>4</sub> was phase-transferred from water to toluene, which is indicated by the color change of the organic layer from colorless to orange. The solution was stirred for 30 min. After all of the Au salt transfers into the organic layer, it was separated from the aqueous layer and

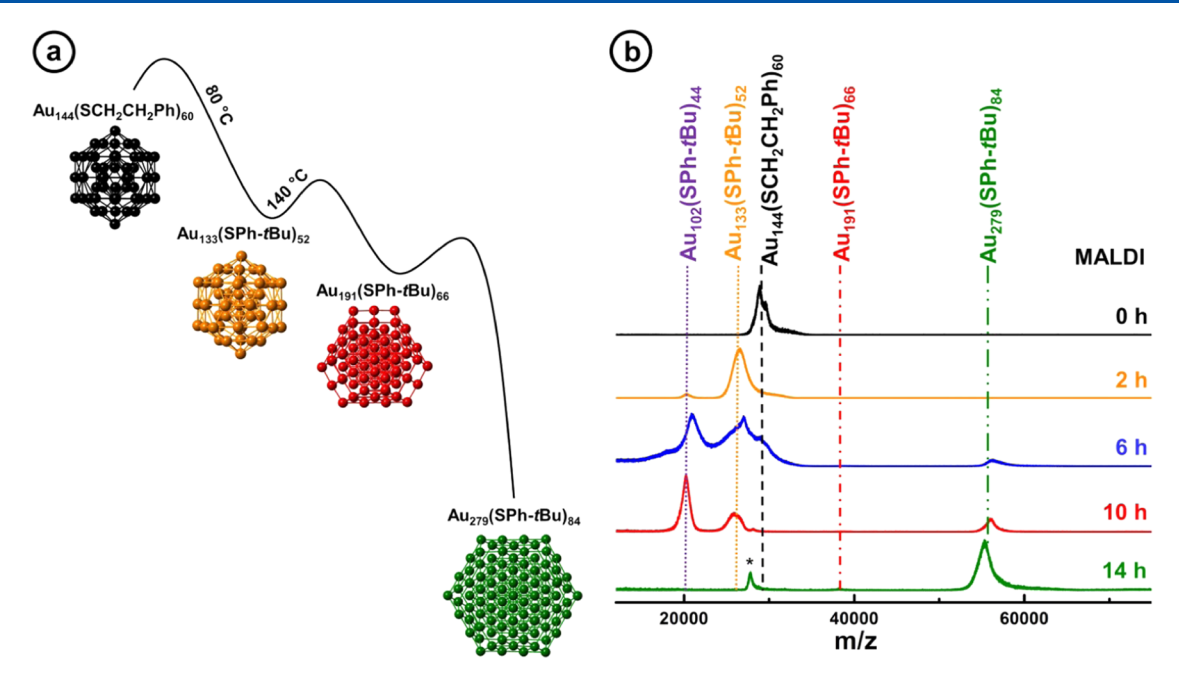


Figure 1. (a) Schematic diagram of the transformation of  $Au_{144}(SCH_2CH_2Ph)_{60}$  to  $Au_{133}(SPh-tBu)_{52}$ ,  $Au_{191}(SPh-tBu)_{66}$ , and  $Au_{279}(SPh-tBu)_{84}$  and (b) MALDI-MS of the starting  $Au_{144}(SCH_2CH_2Ph)_{60}$  and its transformation to  $Au_{133}(SPh-tBu)_{52}$ ,  $Au_{191}(SPh-tBu)_{66}$ , and  $Au_{279}(SPh-tBu)_{84}$  upon reacting with 4-tert-butylbenzenethiol ligand at ~140 °C for 14 h. The dash (black), dot (purple), dot (orange), dash-dot (red), and dash-dot-dot (green) vertical lines correspond to the core mass of  $Au_{144}(SCH_2CH_2Ph)_{60}$ ,  $Au_{102}(SPh-tBu)_{44}$ ,  $Au_{133}(SPh-tBu)_{52}$ ,  $Au_{191}(SPh-tBu)_{66}$ , and  $Au_{279}(SPh-tBu)_{84}$  at high laser, respectively. \* [see first left peak in (b), at 14 h] indicates the +2 charge state of  $Au_{279}(SPh-tBu)_{84}$ .

dipped in an ice bath for another 30 min. Then, phenylethyl thiol was added (Au:thiol = 1:3) to the solution and stirred for 1 h at 1200 rpm. The orange color of the solution changed to white color, indicating the formation of the -Au-SR-Au- polymer. Then, a solution of 0.171 g of NaBH<sub>4</sub> dissolved in 5 mL of ice-cold water was added rapidly to the reaction mixture. The solution turned black, indicating the formation of nanoparticles. The reaction was stirred for 18 h since the NaBH<sub>4</sub> was added to the solution. Then, the reaction mixture was rotary evaporated to remove excess solvent. The crude product was then washed with methanol and water to remove byproducts. Finally, the crude product was extracted to toluene.

Thermochemical Treatment. The crude product was dissolved in toluene and etched in excess phenylethyl thiol at 80 °C with stirring at 600 rpm for 22 h. After that, the excess solvent was rotary evaporated and washed with methanol and water to remove byproducts. Pure  $\mathrm{Au_{144}(SCH_2CH_2Ph)_{60}}$  was isolated by size exclusion chromatography.

Refluxing of  $Au_{144}(SCH_2CH_2Ph)_{60}$  with 4-tert-Butylbenze-nethiol. Pure  $Au_{144}(SCH_2CH_2Ph)_{60}$  was mixed with a 2:1 volume ratio of toluene and 4-tert-butylbenzenethiol and refluxed. Small aliquots of the sample were collected every 2 h, rotary evaporated to remove excess solvents. Then, washed with methanol and water to remove excess thiol, and redissolved in toluene for further analysis.

Computational Thermodynamic Analysis. Both DFTB-MD and the subsequent structural relaxations were performed using the CP2K code. The constrained NVT-MD simulations, lasting 3 ps at 400 K, were based on DFTB Hamiltonians generated with the parameters published in ref 45. The time integration step was 0.5 fs, whereas the temperature was controlled by Nosé-Hoover chain thermostats. Density functional theory (DFT) unrestricted calculations were performed within the Gaussian/plane-wave scheme (GPW).

We employed pseudopotentials derived by Goedecker, Teter, and Hutter<sup>47</sup> for describing the core electrons of all atoms and DZVP basis sets<sup>48</sup> for representing the Kohn–Sham valence orbitals. The cutoff for the auxiliary plane-wave representation of the density was 400 Ry. We took into account dispersive interactions by adding the semiempirical Grimme-D3 correction<sup>49</sup> to the Perdew–Burke–Ernzerhof (PBE)<sup>50</sup> exchange and correlation (xc-) functional.

*Electronic Structure Using DFT.* The electronic structures (including projected densities of states (PDOS)) and atomic (geometrical) structural relaxations of the thiol-ligand-capped gold nanomolecules addressed in this study have been evaluated and analyzed using the density functional theory (DFT) method, employing the Vienna Ab initio Simulation Package VASP. 51-53 The calculations employed a cubic supercell of size 45 Å  $\times$  45 Å  $\times$  45 Å. For the charged cluster ions (see charge states in Figures 5-8), a homogeneous neutralizing background charge has been used. The wavefunctions were expanded in a plane-wave basis with a kinetic energy cutoff of 400 eV. The interaction between the atom cores and the valence electrons was described by the projector augmented-wave (PAW) potential<sup>54</sup> (which includes relativistic corrections), and the exchange—correlation functional was described by the Perdew-Wang PW91 generalized gradient approximation (GGA).<sup>56-58</sup> Van der Waals interactions have been included following ref 59.

# RESULTS AND DISCUSSION

The ligand exchange and core size conversion of  $Au_{144}(SCH_2CH_2Ph)_{60}$  to  $Au_{133}(SPh\text{-}tBu)_{52}$  and then transformation to larger sizes under reflux (Figure 1a) could be readily observed by the MALDI-MS. Typically,  $Au_{144}(SCH_2CH_2Ph)_{60}$  transforms to  $Au_{133}(SPh\text{-}tBu)_{52}$  at 80 °C in the presence of excess 4-tert-butylbenzenethiol (TBBT) $^{30}$  and further transformations were not observed;

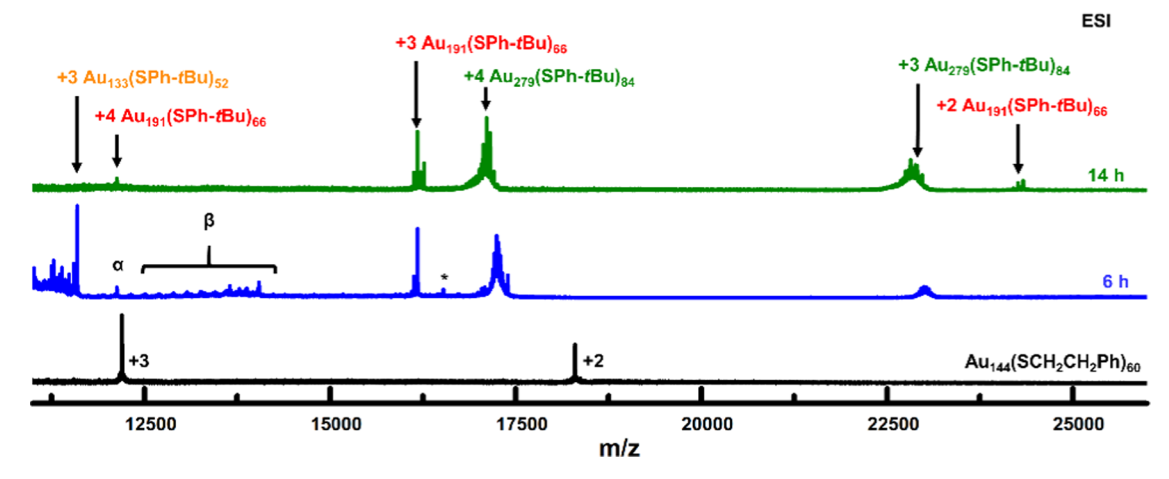


Figure 2. ESI-MS of the starting  $Au_{144}(SCH_2CH_2Ph)_{60}$  at 0 h and its transformation to  $Au_{133}(SPh-tBu)_{52}$ ,  $Au_{191}(SPh-tBu)_{66}$ , and  $Au_{279}(SPh-tBu)_{84}$  upon reacting with 4-tert-butylbenzenethiol ligand at ~140 °C for 14 h. At 6 h,  $Au_{144}(SCH_2CH_2Ph)_{60}$  completely transformed to  $Au_{133}(SPh-tBu)_{52}$ ,  $Au_{191}(SPh-tBu)_{66}$ , and  $Au_{279}(SPh-tBu)_{84}$ . Within 14 h,  $Au_{133}(SPh-tBu)_{52}$  is completely transformed to  $Au_{191}(SPh-tBu)_{66}$  and  $Au_{279}(SPh-tBu)_{84}$ . Within 14 h,  $Au_{133}(SPh-tBu)_{52}$  is completely transformed to  $Au_{191}(SPh-tBu)_{66}$  and  $Au_{279}(SPh-tBu)_{66}$ , and β contains the +2 charge state of  $Au_{98-104}(SPh-tBu)_{39-46}$  clusters. \* indicates the unidentified exchange peaks. For more details, see Figures S3, S4, and S5. Baseline correction for the spectra was done by polynomial fitting.

see Figure S1 for more details. However, when the reaction mixture was placed under refluxing conditions, the reaction was found to advance forward, forming Au<sub>102</sub>(SPh-*t*Bu)<sub>44</sub>, Au<sub>191</sub>(SPh-*t*Bu)<sub>66</sub>, and Au<sub>279</sub>(SPh-*t*Bu)<sub>84</sub>.

The key variables for the size transformation by ligand exchange are temperature, concentration of the reactants, and reaction time. 60 The reorganization of the AuNMs to yield a new structure with the exogenous capping thiol entails the overcoming of an activation energy barrier. <sup>31,60</sup> This energy is supplied as heat, thereby leading to the formation of different end products. 35,37 Au<sub>144</sub>(SCH<sub>2</sub>CH<sub>2</sub>Ph)<sub>60</sub> demonstrates this process by yielding Au<sub>133</sub>(SPh-tBu)<sub>52</sub> at 80 °C when reacting with excess 4-tert-butylbenzenethiol.<sup>30</sup> Under refluxing conditions (~140 °C), larger capped AuNM core sizes,  $Au_{191}(SPh-tBu)_{66}$  and  $Au_{279}(SPh-tBu)_{84}$ , are formed. The activation energy barrier is higher for the larger clusters. Therefore, it requires higher temperatures to transform into larger core sizes. The conversion of Au<sub>144</sub>(SCH<sub>2</sub>CH<sub>2</sub>Ph)<sub>60</sub> to Au<sub>133</sub>(SPh-tBu)<sub>52</sub> and then transformations of Au<sub>133</sub>(SPh $tBu)_{52}$  to  $Au_{102}(SPh-tBu)_{44}$ ,  $Au_{191}(SPh-tBu)_{66}$ , and  $Au_{279}(SPh-tBu)_{66}$ tBu)<sub>84</sub> were monitored using MALDI-MS and UV-vis spectroscopy. ESI-MS was used to determine the composition of the AuNMs in the mixture.

Figures 1b and S2 show the high laser MALDI-MS of the samples collected at each time interval. These figures clearly show the core conversion of Au<sub>144</sub>(SCH<sub>2</sub>CH<sub>2</sub>Ph)<sub>60</sub> to  $Au_{133}(SPh-tBu)_{52}$ , followed by  $Au_{102}(SPh-tBu)_{44}$ ,  $Au_{191}(SPh-tBu)_{44}$ tBu)<sub>66</sub>, and Au<sub>279</sub>(SPh-tBu)<sub>84</sub>; note the undetectability of a signal corresponding to the ligated Au<sub>191</sub> cluster in the MALDI-MS data, attributable to ionization-induced fragmentation of that cluster, thus necessitating identification through the use of the ESI-MS technique operating under milder ionization conditions (see Figure 2, and related discussion, below). From Figures 1 and S2, we observe that, at the start of the process (0 h), the only AuNM species present was Au<sub>144</sub>(SCH<sub>2</sub>CH<sub>2</sub>Ph)<sub>60</sub>, which was confirmed by high laser MALDI-MS at 28.8 kDa (Figure 1b). After 2 h, Au<sub>144</sub>(SCH<sub>2</sub>CH<sub>2</sub>Ph)<sub>60</sub> is completely converted into Au<sub>133</sub>(SPh-tBu)<sub>52</sub> (peak centered at 26.5 kDa at high laser MALDI-MS), and simultaneously  $Au_{102}(SPh-tBu)_{44}$  starts to form. After 6 h, Au<sub>279</sub>(SPh-tBu)<sub>84</sub> starts to form, as indicated

by the MALDI-MS peak at 56.2 kDa. At the same time, the  $\mathrm{Au}_{102}(\mathrm{SPh}\text{-}t\mathrm{Bu})_{44}$  peak became intense. After 10 h, the  $\mathrm{Au}_{279}(\mathrm{SPh}\text{-}t\mathrm{Bu})_{84}$  and  $\mathrm{Au}_{102}(\mathrm{SPh}\text{-}t\mathrm{Bu})_{44}$  peaks became sharper and the  $\mathrm{Au}_{133}(\mathrm{SPh}\text{-}t\mathrm{Bu})_{52}$  peak greatly decreased, affirming that  $\mathrm{Au}_{279}(\mathrm{SPh}\text{-}t\mathrm{Bu})_{84}$  and  $\mathrm{Au}_{102}(\mathrm{SPh}\text{-}t\mathrm{Bu})_{44}$  were formed at the expense of  $\mathrm{Au}_{133}(\mathrm{SPh}\text{-}t\mathrm{Bu})_{52}$ . After 14 h, all of the  $\mathrm{Au}_{133}(\mathrm{SPh}\text{-}t\mathrm{Bu})_{52}$  converted to mainly the  $\mathrm{Au}_{279}(\mathrm{SPh}\text{-}t\mathrm{Bu})_{84}$ , product, accompanied by a minority of smaller  $\mathrm{Au}_{191}(\mathrm{SPh}\text{-}t\mathrm{Bu})_{66}$  AuNM.

When considering the reaction-time variable of the ligand-exchange-induced size transformation, we observe that at the early stages (6–10 h), the Au<sub>102</sub>(SPh-tBu)<sub>44</sub> AuNM that coexists with other sizes in the reaction mixture (Figure 1b) disappears at a later time due to its reduced stability compared to that of the larger product, Au<sub>279</sub>(SPh-tBu)<sub>84</sub>, particularly at a high temperature and for longer reaction times. Interestingly, the reaction did not stop with Au<sub>279</sub>(SPh-tBu)<sub>84</sub>. Instead, it advanced, forming larger sizes than Au<sub>279</sub>(SPh-tBu)<sub>84</sub>. These are polydisperse species and they have masses greater than 120 kDa. During the first 6 h, the formation of such large sizes is insignificant (Figure S2).

To determine the composition of the intermediates and the converted AuNMs, with higher precision, ESI-MS analysis was performed. ESI-MS is a softer ionization technique where fragmentation is minimized, and thus it does not hinder (or interfere with) the determination of the AuNM composition in the reaction mixture. In comparison, MALDI-MS is considered as a hard ionization technique where fragmentation of the AuNMs is observed, with the unwanted complication in the interpretation of the AuNM composition. Figure 2 shows (from bottom to top) the ESI-MS spectra of the starting material (at 0 h), followed by an intermediate stage (at 6 h), and a final stage (at 14 h). The full ESI-MS spectra at each time interval are shown in Figure S3. Figures S4 and S5 are the zoom-in views of the ESI-MS results, showing metastable intermediates of the reaction. Cesium acetate (CsOAc) was added to the AuNM solution to promote ionization. It forms Cs<sup>+</sup> adducts with Cs<sup>+</sup> ions in addition to the molecular peak of

ESI-MS analysis of the starting material shows +2 and +3 charge states of  $Au_{144}(SCH_2CH_2Ph)_{60}$  at 18.3 and 12.2 kDa,

respectively. The absence of any other peaks in the MALDI-MS and ESI-MS spectra confirms the purity of the starting  $Au_{144}(SCH_2CH_2Ph)_{60}$ .  $Au_{133}(SPh-tBu)_{52}$ ,  $Au_{191}(SPh-tBu)_{66}$ and Au<sub>279</sub>(SPh-tBu)<sub>84</sub> peaks emerge at 2 h. But with time, the Au<sub>133</sub>(SPh-tBu)<sub>52</sub> peak reduces, and it disappears at 14 h. The data indicates that the Au<sub>133</sub>(SPh-tBu)<sub>52</sub> was consumed to form  $Au_{191}(SPh-tBu)_{66}$  and  $Au_{279}(SPh-tBu)_{84}$ . At the 6 h mark, there are several peaks present in the reaction mixture, which represent the AuNMs in the Au<sub>98-104</sub>(SPh-tBu)<sub>39-46</sub> cluster size range (Figures 2 and S3). These ESI-MS peaks correlate with the sharp peak observed in the MALDI-MS record at ~20 kDa. As noted above, even though the MALDI-MS signal corresponding to the Au<sub>191</sub>(SPh-tBu)<sub>66</sub> nanomolecule is below the MALDI-MS detection limit, the ESI-MS data shows +2 and +3 charge state peaks corresponding to Au<sub>191</sub>(SPh-tBu)<sub>66</sub>, with one and two Cs<sup>+</sup>-ion adducts (Figure S4 and S5). After 6 h of refluxing, two sets of peak envelopes were observed, corresponding to the +4 and +3 charge states of Au<sub>275-281</sub>(SPh-tBu)<sub>84</sub> (see Figures S4 and S5 for details). After 10 h of refluxing, the peak envelopes were still present, indicating that the reaction does not stop at Au<sub>279</sub>(SPh-tBu)<sub>84</sub> but progresses forward. This progress was also confirmed by comparing the MALDI-MS spectra taken at 6, 10, and 14 h. However, the reaction was stopped after 14 h, as all of the Au<sub>133</sub>(SPh-tBu)<sub>52</sub> was converted to higher sizes.

In the MALDI-MS at 10 h, the most prominent peak is that corresponding to Au<sub>102</sub>(SPh-tBu)<sub>44</sub>, whereas Au<sub>191</sub>(SPh-tBu)<sub>66</sub> is relatively small. By monitoring the ESI-MS at 10 h, the most intense peaks correspond to Au<sub>191</sub>(SPh-tBu)<sub>66</sub> and Au<sub>279</sub>(SPhtBu)84, as these two species ionize well in the ESI-MS compared to Au<sub>102</sub>(SPh-tBu)<sub>44</sub> (Figures 1b and S3). At 14 h, even though the ESI-MS shows the formation of Au<sub>191</sub>(SPhtBu)66, the high laser MALDI-MS indicates that Au<sub>279</sub>(SPhtBu)<sub>84</sub> is the major product. This is a clear illustration that the ESI-MS peak intensity depends on the ionization efficiency of the analyte and not necessarily on the amount of the analyte present in the sample; this observation serves to caution that although the ESI-MS can be used for the identification of species that may be hard to detect with the MALDI-MS technique (because of the aforementioned fragmentation propensity of some of the mixture components under the harsher ionization characteristics of the latter technique, as is the case for the ligated Au<sub>191</sub> nanomolecule, which is predicted to show marginal stability (see theoretical section below), direct comparison of the amounts of analytes determined directly from the ESI-MS data may get complicated due to the differing ionization efficiencies of the analytes.

The optical properties measured with UV—vis absorption spectrum and the calculated photon energy plot (Figure 3a,b, respectively) were used to monitor the reaction progress, as the starting material Au<sub>144</sub>(SCH<sub>2</sub>CH<sub>2</sub>Ph)<sub>60</sub>, and the final product Au<sub>279</sub>(SPh-tBu)<sub>84</sub> has distinct optical properties. The UV—vis spectrum displayed in Figure 3 (black curve at 0 h) shows characteristic optical features for the starting Au<sub>144</sub>(SCH<sub>2</sub>CH<sub>2</sub>Ph)<sub>60</sub> at 510 and 700 nm.<sup>24</sup> The sharp features indicate the high purity of the starting material. The record for Au<sub>133</sub>(SPh-tBu)<sub>52</sub> shown in Figure S6 exhibits features at 510 and 430 nm; the peak at 510 nm is not the plasmonic peak as the absorbance was collected for pure Au<sub>133</sub>(SPh-tBu)<sub>52</sub> where no larger clusters are present. Refluxing Au<sub>144</sub>(SCH<sub>2</sub>CH<sub>2</sub>Ph)<sub>60</sub> with 4-tert-Butylbenzenethiol for 14 h shows a gradual increase of the characteristic peak corresponding to the surface plasmon resonance at 510 nm.

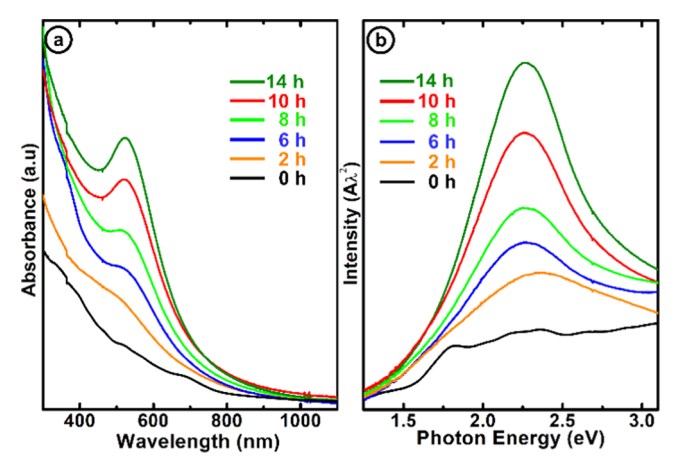


**Figure 3.** (a) UV—vis absorption spectra and (b) photon energy plot of the starting  $\text{Au}_{144}(\text{SCH}_2\text{CH}_2\text{Ph})_{60}$  and its transformation to  $\text{Au}_{133}(\text{SPh}\text{-}t\text{Bu})_{52}$ ,  $\text{Au}_{191}(\text{SPh}\text{-}t\text{Bu})_{66}$ , and  $\text{Au}_{279}(\text{SPh}\text{-}t\text{Bu})_{84}$  at different time intervals. Black at 0 h shows the  $\text{Au}_{144}(\text{SCH}_2\text{CH}_2\text{Ph})_{60}$  features, orange at 2 h, blue at 6 h, light green at 8 h, red at 10 h, and dark green at 14 h. The spectra show the development of plasmonic feature with time, which is an indication of formation of  $\text{Au}_{279}(\text{SPh}\text{-}t\text{Bu})_{84}$ .

This data provides clear evidence for the formation of largersize metallic AuNMs from smaller sizes.

Crystal Structures of  $Au_{144}(SCH_2Ph)_{60}$ ,  $Au_{133}(SPhtBu)_{52}$ ,  $Au_{191}(SPh-tBu)_{66}$ , and  $Au_{279}(SPh-tBu)_{84}$ . An AuNP crystal structure is composed of a metallic core encapsulated by thiolate ligands. An inner core, where only metallic bonds are found, is followed by core surface where Au-S bonds are present. The Au-S bonds can be staples (monomeric [SR-Au-SR], dimeric [SR-Au-SR-Au-SR], trimeric [SR-Au-SR-Au-SR-Au-SR], etc.), or simply bridging thiolates. The crystal structures of  $Au_{144}(SCH_2Ph)_{60}$ ,  $Au_{133}(SPh-tBu)_{52}$ ,  $Au_{191}(SPh-tBu)_{66}$ , and  $Au_{279}(SPh-tBu)_{84}$  are given in Figure S7.

In 2018, the  $\mathrm{Au_{144}(SR)_{60}}$  crystal structure was published with  $\mathrm{HSCH_2Ph}$  as the capping ligand. The crystal is highly symmetric, which is not necessarily the case in other AuNM crystals. The first atomic shell is a hollow  $\mathrm{Au_{12}}$  icosahedron, lacking a central Au atom. The second shell is made of 42 Au atoms, which together with the innermost shell gives rise to the 54-atom Mackay icosahedral structure. The next shell is  $\mathrm{Au_{600}}$ , which builds the rhombicosidodecahedron. On this shell rests the 30 monomeric staples, SR-Au-SR, completing the  $\mathrm{Au_{144}}$  structure. Block-like crystals for  $\mathrm{Au_{144}(SR)_{600}}$ , where  $\mathrm{SR} = \mathrm{SCH_2CH_2Ph}$ , were obtained, but the crystal structure was unresolvable. The However, according to the powder XRD, both show similar atomic structures.

The  $\mathrm{Au_{133}}(\mathrm{SPh}\text{-}t\mathrm{Bu})_{52}$  nanocluster exhibits a structure similar to that of  $\mathrm{Au_{144}}(\mathrm{SCH_2Ph})_{60}$  with few differences. The first shell is an  $\mathrm{Au_{13}}$  icosahedron with a central atom unlike the  $\mathrm{Au_{144}}(\mathrm{SCH_2Ph})_{60}$  structure. The second shell is  $\mathrm{Au_{42}}$  icosahedron, which builds to form the SS-atom Mackay icosahedron. The next shell is  $\mathrm{Au_{52}}$ , which forms the 107-atom core. The final shell is made of 26 monomeric staples protecting the  $\mathrm{Au_{107}}$  core.

The  $Au_{191}(SPh-tBu)_{66}$  crystalline buildup is a rather contrasting structure to those of  $Au_{144}(SCH_2Ph)_{60}$  and  $Au_{133}(SPh-tBu)_{52}$ . It has 26-atom hexagonal close-packed kernel with three center atoms. Following that, the next atomic shells are  $Au_{63}$  and  $Au_{66}$ ; the combined  $Au_{26}$  and  $Au_{63}$ 

shells constitute a mono-twinned  $D_{3h}$  FCC Au<sub>89</sub> inner core.<sup>18</sup> The Au<sub>155</sub> core is protected by 24 monomeric and 6 dimeric staples. The monomeric staples are distributed as 12 on the poles, 6 on the body and 6 on the equatorial position, where the dimeric staples are exclusively on the trapezoidal facets.<sup>18</sup>

The  $\mathrm{Au_{279}}(\mathrm{SPh}\text{-}t\mathrm{Bu})_{84}$  nanocrystallite is also assembled in shells. The first shell is an  $\mathrm{Au_{13}}$  cuboctahedron with a central Au atom. The form the Au<sub>13</sub> Au<sub>42</sub>, and Au<sub>92</sub> shells form an  $\mathrm{Au_{147}}$  FCC cuboctahedral inner core. Together with the  $\mathrm{Au_{102}}$  shell, it forms the TO+249 atom core. This  $\mathrm{Au_{249}}$  core is protected by 18 monomeric staples, 6 dimeric staples, and 30 bridging ligands which completes the  $\mathrm{Au_{279}}(\mathrm{SPh}\text{-}t\mathrm{Bu})_{84}$  structure.

When a capped AuNM is subjected to thermochemical treatment in the presence of an exogenous thiol, the ensuing transformation starts from the outer ligand shell to the inner metallic Au core, and it stops when the stress induced by the tension (strain) associated by the surface ligand exchange processes can no longer penetrate into the AuNM structure and bring about a further structural rearrangement. 60 It has been conjectured that for the transformation to happen the endogenous ligand (outgoing) and the exogenous ligand (incoming) should be characterized as having a significant structural difference.<sup>60</sup> Considering the reaction in our study as a step-wise process, the transformation of  $Au_{144}(SCH_2CH_2Ph)_{60}$  to  $Au_{133}(SPh-tBu)_{52}$  follows the above conjectured trend, whereas the transformation from  $Au_{133}(SPh-tBu)_{52}$  to  $Au_{191}(SPh-tBu)_{66}$  and  $Au_{279}(SPh-tBu)_{84}$ differs.

Theoretical Simulations on the Thermodynamic Stability of Au<sub>144</sub>(SPh)<sub>60</sub>, Au<sub>133</sub>(SPh)<sub>52</sub>, Au<sub>191</sub>(SPh)<sub>66</sub>, and Au<sub>279</sub>(SPh)<sub>84</sub>. Theoretical simulations were conducted to obtain information on the thermodynamic stability of the AuNMs here investigated to shed light on their experimentally determined interconversion.

As a first step, we generated structural models related to the four AuNMs observed here: Au<sub>133</sub>(SPh)<sub>52</sub>, Au<sub>144</sub>(SPh)<sub>60</sub>,  $Au_{191}(SPh)_{66}$ , and  $Au_{279}(SPh)_{84}$ , plus two more models of related AuNMs: Au<sub>144</sub>(SCH<sub>2</sub>Ph)<sub>60</sub> and Au<sub>144</sub>(SCH<sub>3</sub>)<sub>60</sub>, that are used in the Supporting Information (SI) to analyze the Au<sub>144</sub>(SR)<sub>60</sub> case in more detail. Note that we uniformly replaced the experimental 4-tert-butylbenzenethiol ligands with simple benzenethiol ligands to reduce the number of atoms in our models and the computational effort significantly, while the Au<sub>144</sub>(SCH<sub>3</sub>)<sub>60</sub> system has been included as an idealized model of the simplest aliphatic Au<sub>144</sub>(SR)<sub>60</sub> NM. These structural models were generated starting from the experimental X-ray crystal structures of the corresponding compounds:  ${\rm Au_{133}(SPh)_{52}}, {\rm ^{16}}$   ${\rm Au_{191}(SPh)_{66}}, {\rm ^{18}}$   ${\rm Au_{279}(SPh)_{84}}, {\rm ^{15}}$  and  ${\rm Au_{144}(SCH_2Ph)_{60}}, {\rm ^{17}}$ —note that the crystal structure of a homologous AuNM,  $Au_{144}[S(C=C)-(o-Ph-F)]_{60}$ , is also available 62 but we do not use it because its ligands are less similar to ours. For Au<sub>144</sub>(SPh-tBu)<sub>60</sub>, that has not been isolated so far, and for Au<sub>144</sub>(SCH<sub>3</sub>)<sub>60</sub>, which is an idealized model, we started from the X-ray coordinates of Au<sub>144</sub>(SCH<sub>2</sub>Ph)<sub>60</sub><sup>17</sup> and modified the ligands accordingly. Starting from these X-ray coordinates, (i) we modified the ligands as needed, (ii) we conducted constrained (frozen AuS fragment) Ab Initio Molecular Dynamics (AIMD) simulations based on DFTB energy and forces, 63 and finally (iii) we took the configurations at the end of the AIMD runs and subjected them to unconstrained local geometry relaxation using the CP2K code<sup>64</sup> as described in more detail in the Computational

Thermodynamic Analysis section. The final structures after geometry relaxation were used in the following step, stability analysis.

We quantify the energetics of transformations among AuNMs using an analysis framework we proposed previously, based on two basic tools: energy decomposition (fragmentation)<sup>65</sup> and system comparison. We recall the basic principles of our analysis, referring to ref 26 for a review and discussion.

In our fragment decomposition approach, the formation energy of an  ${\rm Au_N(SR)_M}$  nanomolecule is partitioned into three components:  $^{26,65}$  (1) cluster fragmentation —  $\Delta E_{\rm fragm}$ ; (2) metal atomization —  $\Delta E_{\rm atmz}$ ; and (3) ligand separation —  $\Delta E_{\rm ligsep}$ . For convenience, we also define corresponding normalized quantities:  $\Delta E_{\rm fragm}/M$ ,  $\Delta E_{\rm atmz}/N$ , and  $\Delta E_{\rm ligsep}/M$ .

These quantities correspond to the reaction energies of the three sequential disaggregation processes of an AuNM:

(1) cluster fragmentation  $-\Delta E_{\rm fragm}$  separates the cluster into two pieces: an  ${\rm Au_N}$  metal core and a "crown" of thiyl radicals, (SR)<sub>M</sub>, where both pieces are frozen in the geometry of the cluster:

$$Au_N(SR)_M \rightarrow Au_N + (SR)_M^{crown} \Delta E_{fragm}$$
 (1)

(2) metal atomization  $-\Delta E_{\rm atmz}$  process partitions the Au<sub>N</sub> metal core into N separated Au atoms:

$$Au_N \rightarrow N Au \Delta E_{atmz}$$
 (2)

(3) ligand separation  $-\Delta E_{\text{ligsep}}$  process transforms the crown of ligands into M separated thiyls in their relaxed geometry:

$$(SR)_{M}^{crown} \rightarrow M(SR)^{relaxed} \Delta E_{ligsep}$$
 (3)

and the sum of these quantities gives us the total energy of the AuNM as per the formula:

$$\begin{split} E_{\rm total} &= \left(-\Delta E_{\rm fragm}/M\right) \times M + \left[-\Delta E_{\rm atmz}/N + E({\rm Au})\right] \\ &\times N + \left[-\Delta E_{\rm ligsep}/M + E({\rm ligand})\right] \times M \end{split} \tag{4}$$

where E(Au) is the energy of a single Au atom and E(ligand) is the energy of a relaxed isolated ligand,  $SR^{relaxed}$ . Note that we conduct our analysis on relaxed and static configurations: this corresponds to modeling at T=0 K, neglecting vibrational and entropic contributions to the free energy.

In Table 1, we report the complete set of raw energy data and the corresponding derived quantities defined in eqs 1–3. This enables a system comparison analysis <sup>26,30,65</sup> of a pair of AuNMs to single out the sources of their relative stability.

Let us start with the pair:  $\mathrm{Au_{133}}(\mathrm{SPh})_{52}$  vs  $\mathrm{Au_{144}}(\mathrm{SPh})_{60}$ . By slightly modifying our system comparison protocol, here, we use the partitioned energetics of  $\mathrm{Au_{133}}(\mathrm{SPh})_{52}$  to construct piece by piece the energy of a fictitious  $\mathrm{Au_{144}}(\mathrm{SPh})_{60}$  cluster corresponding to the transformation of the  $\mathrm{Au_{133}}$  AuNM into the  $\mathrm{Au_{144}}$  AuNM

$$\begin{split} E_{\text{total}}[\text{Au}_{144}(\text{SPh})_{60} & (\text{Au}_{133}(\text{SPh})_{52}] \\ &= (-\Delta E_{\text{fragm}} / 52 - \text{Au}_{133}) \times 60 + [-\Delta E_{\text{atmz}} / 144 - \text{Au}_{144} \\ &+ E(\text{Au})] \times 144 + [-\Delta E_{\text{ligsep}} / 52 - \text{Au}_{133} + E(\text{SPh})] \\ &\times 60 \end{split}$$

Table 1. Electronic Energies of the Various Models and Fragments: Blue, bare energies; Bold, Derived Quantities as Defined in Eqs  $1-3^a$ 

Au <sub>N</sub> (SPh) <sub>M</sub>	Au <sub>133</sub> (SPh) <sub>52</sub>	Au <sub>144</sub> (SPh) <sub>60</sub>	Au <sub>191</sub> (SPh) <sub>66</sub>	Au <sub>279</sub> (SPh) <sub>84</sub>
total: E <sub>total</sub>	-6884.111180	-7628.608652	-9476.037473	-13255.029779
Au-core: Au <sub>N</sub>	-4421.041437	-4787.008528	-6349.792185	-9276.3236179
shell: (SR) <sub>M</sub> crown	-2457.667197	-2835.874338	-3119.397034	-3970.1408041
ligand: SRrelaxed	-47.255025	-47.255025	-47.255025	-47.255025
$\Delta \mathrm{E}_{\mathrm{fragm}}$	5.402546	5.725786	6.848254	8.565357
$\Delta E_{fragm}/M$	0.10390	0.09543	0.10376	0.10200
$\Delta E_{ligsep}$	0.405897	0.572838	0.565384	0.718704
$\Delta E_{ligsep}/M$	0.007806	0.009547	0.008566	0.008556
$\Delta E_{atmz}/N$	0.096575	0.098777	0.100647	0.104133

<sup>&</sup>lt;sup>a</sup>The energy of Au atoms is −33.144338 au.

The difference,  $\Delta E$ , (changed in sign) between the energy,  $E_{\rm total}[{\rm Au}_{144}({\rm SPh})_{60} @{\rm Au}_{133}({\rm SPh})_{52}]$ , of this fictitious  ${\rm Au}_{144}({\rm SPh})_{60} @{\rm Au}_{133}({\rm SPh})_{52}$  cluster and the energy of the true  ${\rm Au}_{144}({\rm SPh})_{60}$  cluster, i.e., the reaction energy of the transformation from the fictitious to the true cluster, quantitatively assesses the relative stability of these two AuNMs: a negative  $\Delta E$  implies that it is favorable to transform  ${\rm Au}_{133}$  into  ${\rm Au}_{144}$ , and the opposite for a positive  $\Delta E$ .

For the " $Au_{133}(SPh)_{52} \rightarrow Au_{144}(SPh)_{60}$ " case by evaluating eq 5, we obtain the reaction energy  $\Delta E = E_{\text{total}}(\text{Au}_{144}(\text{SPh})_{60})$  $-E_{\text{total}}[Au_{144}(SPh)_{60} @ Au_{133}(SPh)_{52}] = 10.99 \text{ eV. This } \Delta E_{t}$ being large and positive, tells us that the fictitious  $Au_{144}(SPh)_{60}$   $(SPh)_{52}$  cluster is appreciably more stable than the true Au<sub>144</sub>(SPh)<sub>60</sub> cluster, or equivalently that  $Au_{133}(SPh)_{52}$  is appreciably more stable than  $Au_{144}(SPh)_{60}$ ; see the SI for a more detailed analysis of the Au<sub>144</sub>(SR)<sub>60</sub> case. Note that in eq 5, we have used the metal atomization energy of  $Au_{144}(SPh)_{60}$ ,  $\Delta E_{atmz}/144$ -Au<sub>144</sub>, but we would get a positive  $\Delta E$  of 2.36 eV also using the smaller metal atomization energy of  $Au_{133}(SPh)_{52}$ ,  $\Delta E_{atmz}/133$ - $Au_{133}$ . We thus predict that the transformation from Au<sub>144</sub>(SPh)<sub>60</sub> to Au<sub>133</sub>(SPh)<sub>52</sub> is thermodynamically favorable, in perfect agreement with experimental observations. We can add further details to our analysis and observe that  $Au_{144}(SPh)_{60}$  is superior to  $Au_{133}(SPh)_{52}$  only in the  $\Delta E_{\text{ligsep}}/\text{M}$  component, i.e., in the strength of ligand/ligand interactions. However, ligand/ligand interactions are weakened by an increase in temperature so that the "Au<sub>144</sub>(SPh)<sub>60</sub>  $\rightarrow$  $Au_{133}(SPh)_{52}$ " transformation, already favored at T = 0 K, is predicted to become even more favorable by thermal treatment, again in perfect agreement with experimental observations.

Let us now consider the pair:  $Au_{133}(SPh)_{52}$  vs  $Au_{191}(SPh)_{66}$ . By employing the above approach (still transforming the smaller into the larger cluster), we evaluate the energy of a fictitious  $Au_{191}(SPh)_{66}$  cluster built using the energetics of the smaller  $Au_{133}(SPh)_{52}$ 

$$\begin{split} E_{\text{total}}[\text{Au}_{191}(\text{SPh})_{66} & @\text{Au}_{133}(\text{SPh})_{52}] \\ &= (-\Delta E_{\text{fragm}} / 52 - \text{Au}_{133}) \times 66 + [-\Delta E_{\text{atmz}} / 191 - \text{Au}_{191} \\ &+ E(\text{Au})] \times 191 + [-\Delta E_{\text{ligsep}} / 52 - \text{Au}_{133} + E(\text{SPh})] \\ &\times 66 \end{split}$$

Consequently, we obtain that transforming the fictitious  $\mathrm{Au_{191}(SPh)_{66}@Au_{133}(SPh)_{52}}$  cluster into the true  $\mathrm{Au_{191}(SPh)_{66}}$  cluster is energetically favorable by -1.12 eV, implying that transforming  $\mathrm{Au_{133}(SPh)_{52}}$  to  $\mathrm{Au_{191}(SPh)_{66}}$  is

also predicted to be favorable. The transformation energy  $\Delta E = -1.12~{\rm eV}$  is a modest amount. Indeed, the values of  $\Delta E_{\rm fragm}/M$  for these two clusters are nearly identical, while only the ligand separation energy  $\Delta E_{\rm ligsep}/M$  is about 10% larger for  ${\rm Au_{191}(SPh)_{66}}$ . In short, we predict that  ${\rm Au_{133}(SPh)_{52}}$  transforms to  ${\rm Au_{191}(SPh)_{66}}$  as observed experimentally, although the driving force for this transformation is small.

We then consider the pair:  $Au_{191}(SPh)_{66}$  vs  $Au_{279}(SPh)_{84}$ , and we evaluate the energy of a fictitious  $Au_{279}(SPh)_{84}$  built using the energetics of  $Au_{191}(SPh)_{66}$ 

$$\begin{split} E_{\text{total}}[\text{Au}_{279}(\text{SPh})_{84} @\text{Au}_{191}(\text{SPh})_{66}] \\ &= (-\Delta E_{\text{fragm}}/66 - \text{Au}_{191}) \times 84 + [-\Delta E_{\text{atmz}}/279 - \text{Au}_{279} \\ &+ E(\text{Au})] \times 279 + [-\Delta E_{\text{ligsep}}/66 - \text{Au}_{191} + E(\text{SPh})] \\ &\times 84 \end{split}$$

From the above, we obtain that transforming the fictitious  $Au_{279}(SPh)_{84} @Au_{191}(SPh)_{66}$  cluster into the true  $Au_{279}(SPh)_{84}$ cluster is energetically unfavorable by  $\Delta E = 4.11$  eV. This  $\Delta E$ is due essentially to the fact that  $\Delta E_{\rm fragm}/M$  is about 1.7% larger for Au<sub>191</sub>(SPh)<sub>66</sub> than for Au<sub>279</sub>(SPh)<sub>84</sub>, whereas the values of  $\Delta E_{\text{ligsep}}/M$  for the two AuNMs are nearly identical. However, it is crucial to observe that, using the metal atomization energy of  $Au_{191}(SPh)_{66}$ ,  $\Delta E_{atmz}/191$ - $Au_{191}$ , in eq 8, the order of stability is reversed in favor of  $Au_{279}(SPh)_{84}$ , by a large and negative  $\Delta E$  of -22.36 eV for transforming the fictitious  $Au_{279}(SPh)_{84}@Au_{191}(SPh)_{66}$  into the true Au<sub>279</sub>(SPh)<sub>84</sub> cluster. We therefore finally predict that  $Au_{191}(SPh)_{66}$  will transform into  $Au_{279}(SPh)_{84}$ , in agreement with experiment, and that the reason of this greater energetic stability of Au<sub>279</sub>(SPh)<sub>84</sub> is associated with its larger and more stable metallic core. Note that this transformation can be further favored by two effects that are neglected in our analysis: (a) as noted above, at high temperatures, vibrational phenomena in general weaken the contribution of  $\Delta E_{\text{fragm}}/M$ relative to that of  $\Delta E_{\rm atmz}/N$ , and (b) kinetic trapping may favor the more regular  $Au_{279}(SPh)_{84}$  cluster with respect to the stacking faults of Au<sub>191</sub>(SPh)<sub>66</sub> (see the discussion of crystal structures above). Finally, we note in passing that the stronger ligand fragmentation (ligand/core interaction, i.e., ligand adhesion) of Au<sub>191</sub>(SPh)<sub>66</sub> probably contributes to its peculiar optical properties.

In summary, our thermodynamic analysis, as detailed in the Deeper discussion of the Au<sub>144</sub>(SX)<sub>60</sub> vs Au<sub>133</sub>(SX)<sub>52</sub> cases section in the SI, shows that Au<sub>144</sub>(SCH<sub>2</sub>CH<sub>2</sub>Ph)<sub>60</sub> transforms into Au<sub>133</sub>(SPh-tBu)<sub>52</sub> because the differential strength of the Au-S bond in aliphatic vs aromatic ligands (discussed in detail in ref 26) and the greater stability of the larger and less defective metal core in Au<sub>144</sub>(SCH<sub>2</sub>CH<sub>2</sub>Ph)<sub>60</sub> are more than compensated by the much stronger bonding of sparser conjugated thiyls to a defective metal core in Au<sub>133</sub>(SPhtBu)<sub>52</sub>. This initial transformation from Au<sub>144</sub>(SCH<sub>2</sub>CH<sub>2</sub>Ph)<sub>60</sub> into Au<sub>133</sub>(SPh-tBu)<sub>52</sub> is followed by further transformations into Au<sub>191</sub>(SPh-tBu)<sub>66</sub> and Au<sub>279</sub>(SPh-tBu)<sub>84</sub> compounds (where Au<sub>191</sub> is predicted to be only marginally stable due to a stronger ligand/core adhesion), with these processes being driven primarily by the stability-enhancing effect of the more stable metallic cores of these larger species.

Electronic Structure of the Thiolate-Capped Gold Nanomolecules. Insights into the electronic structure and stability of the thiolate-ligand-capped nanomolecules were gained through calculations using the density functional theory

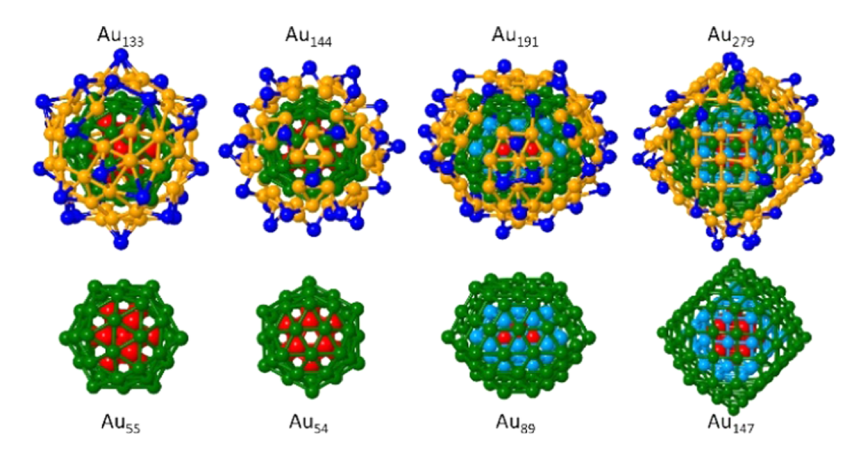


**Figure 4.** Optimized structures of the AuNMs considered in this study. Top row: views of the energy-optimized clusters (starting from the X-ray-determined ones). Only the Au atoms (with the different atomic shells (see the SI), depicted in red, green, and orange) and the S atom (in blue) of the capping thiolate are depicted. Bottom row: relaxed inner cores (ICs) corresponding to the clusters displayed in the top row.

(DFT) method, employing the Vienna Ab initio Simulation Package VASP; 51-55 for further details, see the Method section. All of the results shown below were obtained with the use of these theoretical simulations, subsequent to optimization of the thiolate-capped structures of the gold nanomolecule (starting from the X-ray crystal structures referenced above and in displayed in Figure S7). A summary of the AuNMs' structures (only the metals atoms and the thiolate-anchoring sulfur atoms are shown), as well as the corresponding inner-core (IC) structures (i.e., those atoms of the AuNM that are not bonded directly to the sulfur atoms of the thiol ligands) is shown in Figure 4.

The projected density of states, PDOS, that is, the electronic density of states of the capped AuNMs projected onto the angular momentum components,66 calculated for the Au<sub>n</sub>(SR)<sub>m</sub> nanomolecule (with SR corresponding to the thiolate ligands indicated in the figures)—for (n,m;k): (144,60;54), (133,52;55), (191,66;89), and (279,84;147), where (n,m;k) corresponds to the number of Au atoms (n), number of thiolate ligands (m), and number (k) of Au atoms in the corresponding IC clusters—are shown in Figures 5-8, respectively. In the calculations of the PDOS, we have used the ligands (-SR) indicated in the figures, whereas for the larger sizes (Au<sub>191</sub> and Au<sub>279</sub>), we have employed (for computational convenience) -SPh, rather than S-Ph-tBu. This replacement has been shown previously (see Figures S2B and S2C in ref 19) to have a rather insignificant influence on the PDOS results for sufficiently large clusters (e.g.,  $n \sim 100$ ) particularly in the region of the gap  $\Delta E_{\rm HL}$  between the highest (and lowest) occupied (unoccupied) molecular orbitals, HOMO (LUMO); see the region in Figures 5-8 near the vertical dashed line at  $E-E_{\rm F}=0$ , where  $E_{\rm F}$  is the Fermi level.

The PDOS spectra in Figures 5–8 exhibit a series of peaks color coded according to their angular momentum character, determined via spherical-harmonics  $(Y_{\rm lm})$  expansion of the DFT-calculated eigenfunctions. The features to the left of the above-mentioned  $E-E_{\rm F}=0$  point (marked by a dashed line) correspond to occupied orbitals, and those above it belong to the unoccupied part of the electronic spectrum. The  $\Delta E_{\rm HL}$  gap is the excitation threshold energy. The opening of such gap (and its magnitude) confers the electronic stability to the studied cluster (see below). The organization of the electronic states is analyzed using the cluster-shell-model (CSM) formulated originally in the investigation of simple (e.g.,

alkali) metal clusters, and generalized later to other elements (in particular, coinage metals, e.g., Ag, Au, Pt) in a study of a series of gold nanoclusters, where it has been termed as "the partial jellium model";66 this methodology has been subsequently used in a number of investigations of ligand-capped metal clusters [see, e.g., refs 68 and 69]. As already elaborated elsewhere 18,19,66 for a wide range of energies (located at the middle of the energy spectrum), the electronic wavefunctions exhibit localized character (associated with Au atomic 5d electrons). The orbitals of states with energies near the bottom of the electronic spectrum, as well as near the top of the spectrum (near the Fermi level), are of delocalized character, associated with the atomic Au 6s<sup>1</sup> electrons (see, e.g., orbital images at the top of Figure 5). The organization (occupation ordering) of these delocalized states follows the CSM, or superatom, aufbau scheme, where the electron filling follows the rule: 1S<sup>2</sup>| 1P<sup>6</sup>| 1D<sup>10</sup>| 2S<sup>2</sup>| 1F<sup>14</sup>| 2P<sup>6</sup> 1G<sup>18</sup> |2D<sup>10</sup>1H<sup>22</sup> 3S<sup>2</sup> | 1I<sup>26</sup>..., where S, P, D, F, G, H, and I correspond to angular momenta L = 0, 1, 2, 3, 4, 5, and 6. The shell closures (socalled "magic numbers") are denoted by vertical lines, and closure near  $E_{\rm F}$  is often accompanied by opening of a stabilizing energy gap (referred to as  $\Delta_{HL}$ ). The "magic numbers", that is, the number of electrons completing the shells, take the following values  $n^* = 2, 8, 18, 20, 34, 58, 90, 92$ electrons, and so on; we remark it that clusters with electron occupation close to these magic number are found to also exhibit enhanced electronic stabilization. It should be noted that the above aufbau rule and magic number sequence result from an assumed spherical (or near-spherical) cluster shape. Deviations of the cluster geometry from the assumed spherical shape bring about lifting of the g = 2L + 1 degeneracy of the levels belonging to the L-th angular momentum. In condensedmatter and molecular physics, such degeneracy-lifting is commonly termed as crystal-field level splitting; in general, group theoretical considerations can assist in determining which superatom levels (based on a spherical model and thus characterized, as described above, by their angular momenta L) may be split by a given point-group symmetry of the atomic spatial arrangement in the cluster under study. In an early study, such symmetry-breaking (with the influence of the point-group symmetry associated with the cluster atomic arrangement, treated perturbatively) has been modeled and illustrated<sup>70</sup> for the analysis of the electronic spectrum of the C<sub>60</sub> cluster, and a general discussion of metal-cluster shape

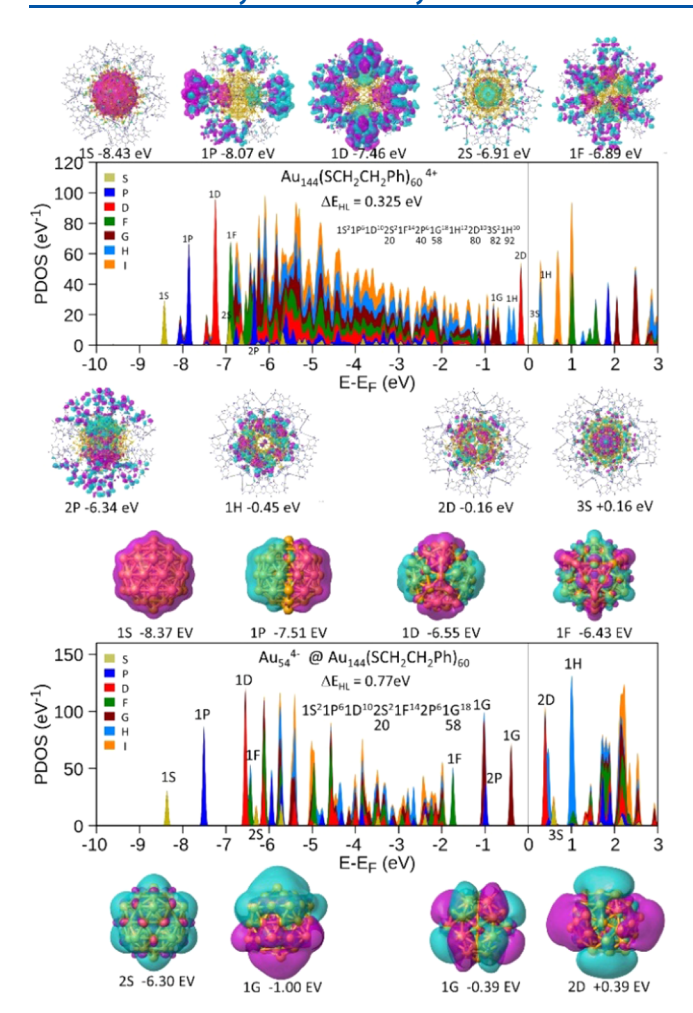


Figure 5. Electronic structure of the optimized  $Au_{144}(SCH_2CH_2Ph)_{60}$  nanomolecule (in the 4+ charge state, top panel) and for the relaxed inner-core cluster  $Au_{54}$  @ (S-CH<sub>2</sub>CH<sub>2</sub>Ph)<sub>60</sub> in the molecule. Displayed in both panels are the calculated PDOS, with the various angular momenta contributions shown in different colors, as given in the inset in the top panel. Also shown above and below each panel are isosurfaces of selected (delocalized) superatom electronic orbitals corresponding to the indicated angular momenta (e.g., 1S, 1P, 1D, etc.), which make up the electronic shell structure of the cluster; see aufbau list in the top and bottom panels, with the corresponding electron fillings indicated underneath. Note the crystal-field splitting of the 1H level near the Fermi level in the upper panel. The highest occupied molecular orbital (HOMO)—lowest unoccupied molecular orbital (LUMO) gaps for the 144-gold atom AuNM (Δ<sub>HL</sub> = 0.325 eV) and for the 54 Au atom inner core ( $\Delta_{\rm HL}$  = 0.77 eV) are indicated.

effects on the electronic shell model can be found in ref 71. We remark here that the above effects of the cluster atomic geometrical (crystallographic) structure may lead to certain reordering of the superatom orbitals, especially near the top of the occupied spectrum; compare, e.g., the ordering of the 1G, 1H, and 2D superatom levels near  $E - E_{\rm F} = 0$  in the top panels of Figures 5 and 6.

The PDOS spectrum of the energy-optimized X-ray structure exhibited in the top panel of Figure 5 for the starting AuNM Au<sub>144</sub>(SCH<sub>2</sub>CH<sub>2</sub>Ph)<sub>60</sub> shows a relatively small HOMO–LUMO gap ( $\Delta_{\rm HL}=0.325$  eV). Examination of the electronic structure—see in particular the isosurfaces of selected orbitals displayed above and below the top panel of Figure 5, corresponding to peaks in the PDOS spectrum at the indicated

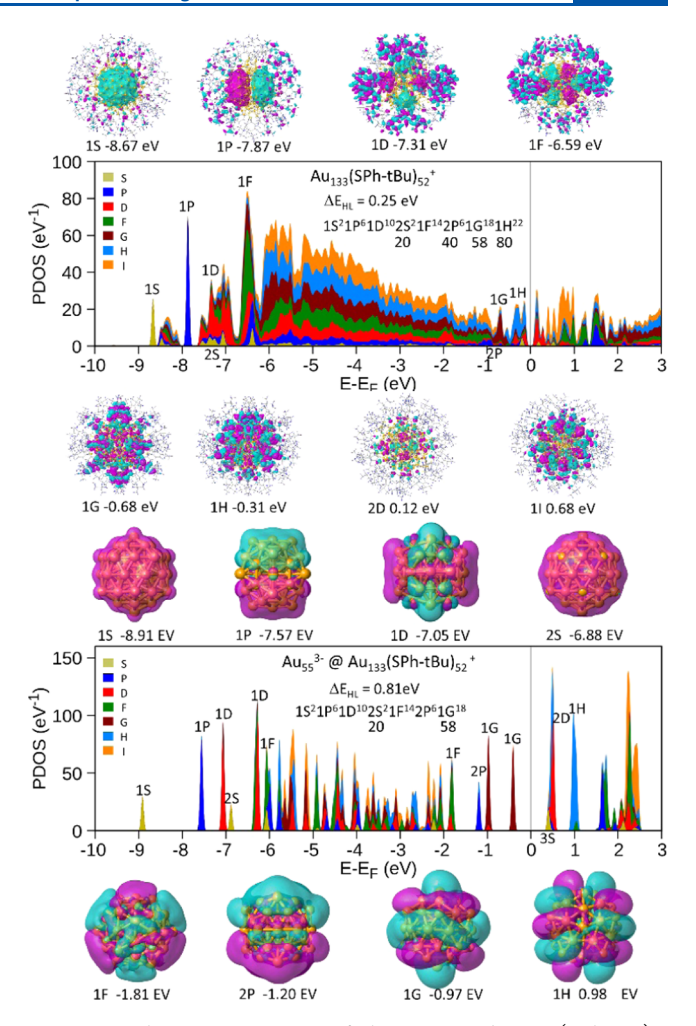


Figure 6. Electronic structure of the optimized  ${\rm Au_{133}(SPh\text{-}tBu)_{52}}$  nanomolecule (in the 1+ charge state, top panel) and for the relaxed inner-core cluster  ${\rm Au_{55}}$  in the charge state 3-. Displayed in both panels are the calculated PDOS, with the various angular momenta contributions shown in different colors, as given in the inset in the top panel. Also shown above and below each panel are isosurfaces of selected (delocalized) superatom electronic orbitals corresponding to the indicated angular momenta (e.g., 1S, 1P, 1D,....), which make up the electronic shell structure of the cluster; see aufbau list in the top and bottom panels, with the corresponding electron fillings indicated underneath. Note the crystal-field splitting of the 1H level near the Fermi level in the top panel. The HOMO–LUMO gaps for the 133-gold atom AuNM ( ${\rm \Delta_{HL}}=0.25~{\rm eV}$ ), and for the 55 Au atom inner core ( ${\rm \Delta_{HL}}=0.81~{\rm eV}$ ) are indicated.

energies—provides clear evidence for delocalized (superatom states with eigenenergies lying at the bottom and top (near the HL gap) of the PDOS spectrum, in agreement with the aforementioned "partial jellium" model). We also call attention to the energy splitting of the 1G and 1H at the top of the spectrum, caused by the above-mentioned crystal-field effects and interactions with the ligand capping environment, with parts of the split orbitals being occupied by the delocalized electrons and some lying above the gap (in the unoccupied manifold). The aufbau orbital-filling scheme shown in Figure 5 indicates shell-closing by 80 electrons with a fully occupied (10 electrons) 2D HOMO orbital.

We devote attention to the computationally predicted energy splitting of 1G and 1H at the top of the spectrum, caused by the above-mentioned effects of the crystalline

structure (with the symmetry of the atomic arrangement in the cluster entering the first-principles DFT calculations through the electron-metal-ion interaction potential, which reflects the point-group symmetry of the cluster atomic structure), and interactions with the ligands capping environment; note that for the ligated Au<sub>144</sub> cluster (in the crystallographically determined structure, see the top panel in Figure 5), all of the split 1G levels lie in the occupied manifold, whereas only part of the 1H split levels is occupied by the delocalized electrons and some of the split levels are located above the gap (in the unoccupied manifold). When modeled, using the crystal-field perturbative approach, 70 the degree of superatom degeneracy lifting that underlies level splitting is governed by matrix elements of the atomic structure perturbing potential (expressing the point-group symmetry of the atomic arrangement in the cluster) and on the angular momentum symmetry of the superatom orbital being considered.

Further insight into the electronic structure of the cluster is gained through analysis, which we introduced recently as the "core-cluster-shell model" (CCSM). <sup>18,19</sup> In this model, one explores stabilization (reflected by opening of a relatively large  $\Delta_{HL}$  gap) that results from the organization of the superatom (shell) electronic energy levels corresponding to delocalized electrons of the metal atoms (6s1 electrons for Au) that reside in the inner-core region of the ligand-capped nanoparticle (i.e., metal atoms not bonded directly to the capping thiols). For the 144-gold atom AuNM, this IC is denoted as Au<sub>54</sub>-@ Au, (SCH<sub>2</sub>CH<sub>2</sub>Ph) and the PDOS spectrum for that IC in a four-charge state is displayed in the bottom panel of Figure 5. This IC (relaxed) cluster exhibits a large stabilization energy gap ( $\Delta_{HL} = 0.77 \text{ eV}$ ), with no splittings at the top of the spectrum. The aufbau orbital-filling scheme shown in the figure indicates shell closure at a magic number of 58 electrons, with the HOMO orbital being a full  $1G^{18}$  (L = 4) orbital (see also the isosurface shown at the bottom of the lower panel of Figure 5). As we discussed previously, <sup>18,19</sup> as well as from the analysis that we present below (particularly for the n = 191 and n = 279 AuNMs), the CCMS methodology proves most useful for cases where only a small or no  $\Delta_{HL}$  gap and no delocalized superatom orbitals near the Fermi level are found in the density of states of the entire capped nanoparticle. Moreover, the CCSM model is motivated by considerations relating to the cluster growth process, where one expects that the electronic and geometric stability of the earlier-formed nucleating inner core of the metal nanoparticle (particularly stabilization of that IC due to its emergent superatom shell structure) would confer stabilization to the (subsequently assembling) outer atomic shells that anchor the capping organic ligands. We remark, however, that outer-shell stress generated by ligand-exchange transformations (such as those discussed in this paper), may induce structural transformations of the inner-core.

Applying such analysis to the calculated PDOS spectra for the  $Au_n(SR)_m$  nanomolecules (with SR = SPh-tBu or SPh, as indicated), for the AuNM transformation product,  $Au_n(SR)_m$  with (n,m;k): (133,52;55), (191,66;89), and (279,84;147), where k corresponds to the number of gold atoms in the IC  $Au_k @ Au_n(SR)_m$  (with the charge states as indicated in Figures 6–8 for n = 133, 191, and 279, respectively), we observe the following trends:

(1) The stabilization gaps of the transformation products decrease with cluster size:  $\Delta_{\rm HL} = 0.25$  eV (n = 133); 0.16

eV (n = 191); and 0.05 eV (n = 279), with the delocalized superatom orbitals at the top of the occupied spectrum (near the gap) largely obliterate two larger clusters (see Figures 7 and 8).

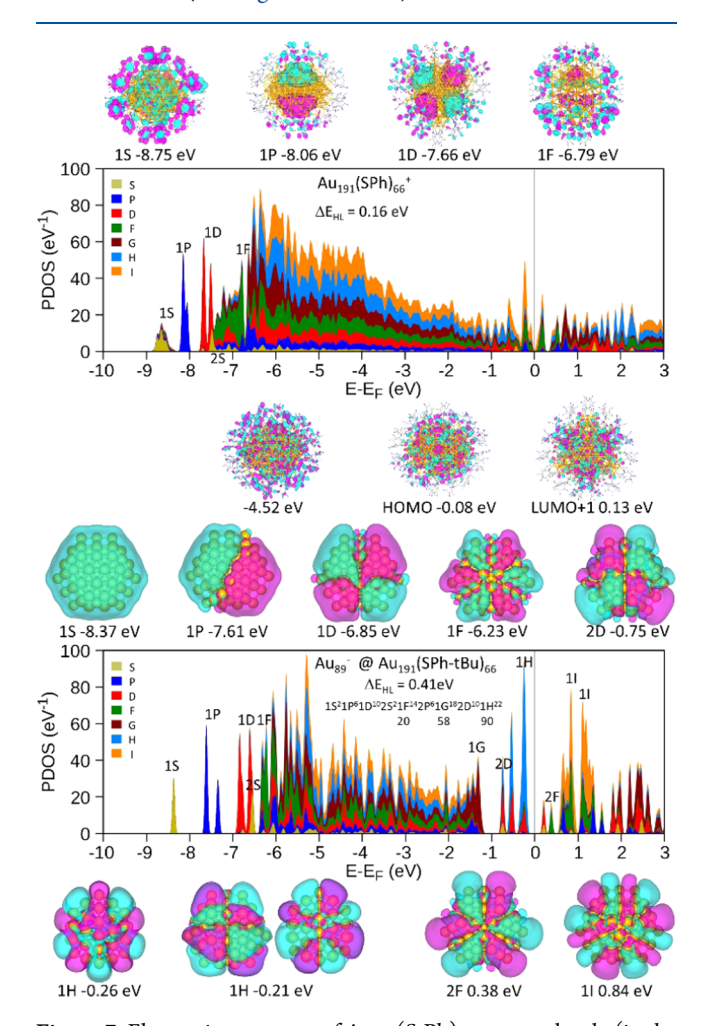
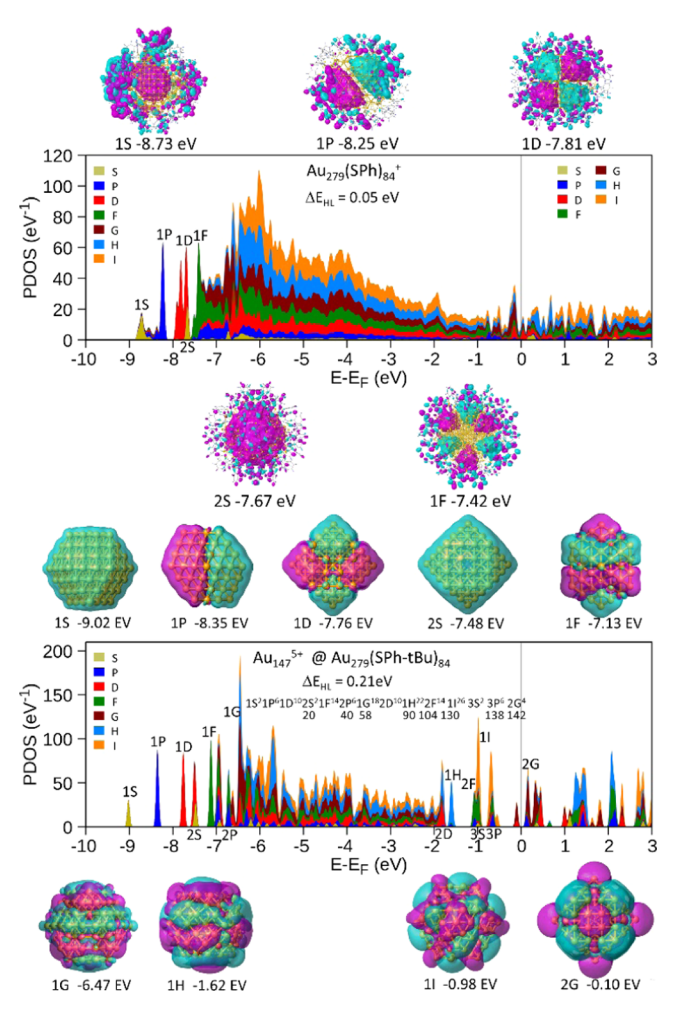


Figure 7. Electronic structures of Au<sub>191</sub>(S-Ph)<sub>66</sub> nanomolecule (in the charge state 1+, top panel) and the relaxed IC cluster (in the 1- charge state) Au<sub>89</sub> @Au<sub>191</sub> (S-phenyl-tBu)<sub>66</sub>. Calculated Projected densities of states (PDOS) are shown in the two panels (color coded as shown in the inset to the top panel). Also displayed above and below the PDOS plots are isosurfaces of orbitals of selected electronic states of the ligand-capped cluster. The 1S, 1P, 1D, and 1F orbitals shown above the top panel (all corresponding to states at the bottom part of the PDOS spectrum) display delocalized, superatom, characteristics. On the other hand, the orbitals shown below the top panel, corresponding to the marked energies, are of localized nature, and any symmetry that they display reflects that of the atomic arrangements, reflecting structural symmetry (note, in particular, the ones near the Fermi level). Fot the IC, the isosurfaces (above and below the bottom panel) all show delocalized superatom character.  $\Delta_{HL}$  = 0.16 eV for the capped 191 Au cluster (top) and 0.41 eV for the IC (bottom). Figure adapted from ref 18.

(2) A clear stabilization gap characterizes the relaxed ICs Au<sub>k</sub>@Au<sub>n</sub>(SR)<sub>m</sub> (in the charge states indicated in Figures 6–8, respectively): Δ<sub>HL</sub> = 0.81 eV (k = 55, n = 133); 0.41 eV (k = 89, n = 191); and 0.21 eV (k = 147, n = 279). Added stability of the ICs is of geometric (packing) origin. Indeed, the multitwinned IC with k = 55 (n = 133)<sup>16</sup> (and the IC with k = 54 of the starting Au<sub>144</sub>(SCH<sub>2</sub>CH<sub>2</sub>Ph)<sub>60</sub>AuNM), the mono-twinned FCC



**Figure 8.** Electronic structure of  $Au_{279}(S-Ph)_{84}$  nanomolecule (in the charge state 1+, top panel) and of the relaxed IC cluster (in the 5+ charge state)  $Au_{147}^{-}$  (@ $Au_{279}(S-phenyl-tBu)_{84}$ . Calculated projected densities of states (PDOS) are shown in the two panels (color coded as shown in the inset to the upper panel). Also displayed above and below the PDOS plots are isosurfaces of orbitals of selected electronic states of the ligand-capped cluster. The 1S, 1P, 1D, 2S, and 1F orbitals shown above the top panel (all corresponding to states at the bottom of the PDOS spectrum) display delocalized, superatom, characteristics. In contrast, delocalized superatom orbitals near the top of the spectrum (in the gap vicinity) were not discernible. For the relaxed IC, the isosurfaces (above and below the bottom panel) all show delocalized superatom character.  $\Delta_{\rm HL} = 0.05$  eV for the capped 279 Au cluster (top) and 0.21 eV for the IC (bottom).

 $D_{3h}$  cluster<sup>18</sup> found for k=89 (n=191), and the cuboctahedron found for k=147 (n=279)<sup>15</sup> are all known for their structural packing stability. We conclude that the electronic and geometrical structural stabilities of the ICs are likely to serve as contributors to the continued assembly of the outer atomic shells, which anchor the capping passivating ligands.

## CONCLUSIONS

Having given full account of our experimental and theoretical findings that addressed the size and structural transformations brought about by ligand exchange at a high temperature ( $\sim$ 140  $^{\circ}$  C) under reflux conditions, starting with Au<sub>144</sub>(SCH<sub>2</sub>CH<sub>2</sub>Ph)<sub>60</sub> and culminating with Au<sub>279</sub>(SPh-tBu)<sub>84</sub>, we turn now to a discussion of our work and its future

expected impact, in light of the current status of this field of scientific research.

Identification, characterization, and elucidation of the physical and chemical origins of size-dependent evolution of the structure and properties of finite clusters of atoms or molecules are principal goals of cluster science. Coupled to the above are the experimental challenges entailed in the design and implementation of methods of synthesis resulting in the isolation of clusters of specific sizes (i.e., number of atoms), as well as their superlattice assemblies. Although investigations of (gas-phase, free) size-selected clusters in beams have been carried out for close to half a century now, studies on solutionsynthesized well-defined metal clusters of specific sizes started only less than three decades ago. 1,2,72 The methodology that enabled the emergence and growth of the currently burgeoning field of organically capped metal-cluster nanomolecules (MCNM, MC = Au in the present work) utilized the twophase colloid preparation method of Faraday<sup>73</sup> in conjunction with phase transfer, gold-alkanethiolate chemistry, combined with mass spectrometry (e.g., MALDI-MS) and ESI-MS, as well as optical (UV-vis) spectroscopy and high-resolution electron microscopy (HREM), as primary synthesis and characterization tools. Indeed, the large majority of MCNMs synthesized to date [e.g.,  $Au_n(SR)_{m}$ , where -SR signifies the capping thiolate ligand] have been obtained using this methodology, or variants thereof (see "controlled etching" discussed in ref 74, which was dubbed later<sup>24</sup> as "size focusing"). Furthermore, aiming at effecting functionalization of the metals cores of capped MCNMs, a "place", or "site exchange" strategy<sup>75</sup> has been developed (in analogy to that used in self-assembled monolayers, SAMS, on planar metal surfaces) where some or all of the m alkanethiolate ligands (SR)<sub>m</sub> of an MCNM are exchanged by another alkanethiolate (SR") to form  $Au_n(SR)_{m-x}(SR')_x$ ; note that the size of the inorganic (metal) gold core is maintained throughout.

Already early theoretical investigations 1,76,77 pertaining to the size evolution of the structures of atomic clusters (capped metal clusters, in particular) showed clear evidence for the nonmonotonous pattern traced by the energetics and stability, as well as other properties, of the metal cores of such AuNMs, with respect to their sizes; the nonmonotonous nature of the properties of bare gas-phase clusters, exhibited in their measured and calculated abundances, energetic stability, ionization potentials, electron affinities, chemical properties, and melting temperatures, has been realized even earlier.<sup>67,71</sup> Indeed, for the case of capped AuNMs, the characteristic energy (per atom) of the gold cores corresponding to AuNMs of varying size (number of core Au atoms) was predicted to exhibit a discrete sequence of minima, corresponding to aggregation of the atoms into polyhedra with varying structural motifs (e.g., octahedra, Ino-decahedra, Marks' decahedra, icosahedra, etc.) with perfect symmetries or variants thereof. This has been summarized in ref 1 as follows: "In summary, through the use of surfactants (self-assembled monolayers) that are capable of etching imperfect structures and of passivating crystal facets in a compact manner compatible with the underlying crystallite surface structure, one is led to highly stable and versatile molecular nanocrystal materials" and "Evidence for the formation of such a discrete sequence of nanocrystal gold molecules, rather than the appearance of a continuous distribution of sizes and structures, has been established and confirmed through independent measurements, including: size-segregation in precipitation of mixed

samples; mass spectrometric detection capable of resolving even small (less than 10%) quantities of species differing in size by less than one lattice spacing; invariance of the sequence and observed properties to the details of the preparation and separation procedures, and structural analyses performed on isolated fractions of the sequence, guided by, and correlated with, theoretical predictions. The discrete nature and stability of such nanocrystal materials and the size-evolutionary patterns of their properties, including their propensity to form extended superlattices, suggest ways and means for the design and fabrication of advanced optical, electronic, (photo)catalytic and sensor materials of controlled characteristics".

The discrete nature of the size evolution and the synthesis method discussed above serve as background of our discussion of the methodology employed and further developed in this work, namely, the ligand-exchange-driven core size and structure transformation chemistry explored in this work. This methodology aims at accessing stable AuNMs with varying precise core sizes, starting from a stable "precursor" characterized by a different number of core Au atoms. This is achieved via thermally activated ligand exchange-induced structural (and/or size) transformation, with the incoming (exogenous) ligand being different from the one capping the precursor AuNM; it is reasonable to assume 60 mechanistically, the transformation will propagate from the outer capping ligand shell inward toward to the metallic core [thus bringing about structural change induced by the (surface) ligand-exchange process], and consequently, it is expected (and indeed found) that the activation energy of the structural transformation of the metallic core would increase with the AuNM core size, thus requiring higher operating temperatures for larger ones. As noted in the Introduction section, in this process, the AuNM reaches a new thermodynamically stable structure upon heating with an exogenous thiol. This transformation occurs with the loss or gain of Au atoms in the course of the ligand exchange process. 30,31,33 The number of ligands may or may not change in the course of conversion. We note here that in the initial report on core size transformation driven by a ligand exchange, the reaction of an aromatic ligand (benezene thiolate, SPh) was used as the exogenous ligand acting on a phenylethanethiolate (PET)-protected 15-25 kDa mixture, resulting in an Au<sub>36</sub>(SPh)<sub>23</sub> product. In subsequent work, the first exchange reaction starting from an atomically precise precursor (Au<sub>38</sub>(PET)<sub>24</sub>) and resulting in a high yield (>90%) of  $Au_{36}(TBBT)_{24}$  (TBBT = tetrabutylbenzene thiol) has been reported, and the X-ray structure was determined.<sup>36</sup> Most of the ligand-exchange-driven size transformations performed to date have been limited to AuNMs with less than 100 Au atoms (mostly 20-50 atoms),60 with only very few exceptions including the transformations of ligated Au<sub>144</sub> to a smaller ligated Au<sub>133</sub> AuNM, in refs 30 and 79.

In light of the above, we set as our goal in this study to explore the ligand-exchange-driven size and structure transformations to sizes that are significantly larger than those that have been realized previously. To this aim, we established first that a size conversion of an atomically precise 144-Au precursor cluster capped by PET,  $\mathrm{Au_{144}(SCH_2CH_2Ph)_{60}}$ , yields an AuNM with a smaller gold core  $(\mathrm{Au_{133}(SPh\text{-}tBu)_{52}})$  when reacted with TBBT at 80 °C. However, when the initial precursor is treated (heated) with TBBT under reflux conditions (allowing for a much higher temperature of 140 °C), in addition to the previously observed TBBT-capped

Au<sub>133</sub> product AuNM, larger capped gold nanomolecular core sizes, i.e.,  $\mathrm{Au_{191}(SPh\text{-}tBu)_{66}}$  and  $\mathrm{Au_{279}(SPh\text{-}tBu)_{84}}$ , were detected, along with  $\mathrm{Au_{102}(SPh\text{-}tBu)_{44}}$  that has been observed as an intermediate, disappearing after 10 h of refluxing due to its lesser stability at a high temperature for longer reaction times. These core conversions were monitored at various times (up to 14 h) during the size and structure conversion process, with the use of MALDI-MS, ESI-MS, and UV—vis spectroscopy.

Concurrent with the experimental findings, we have carried out theoretical explorations, involving DFT-based fragment decomposition analysis<sup>26</sup> of the ligand-capped AuNMs formation energies, identifying the energetic contributions (gold metallic core, anchoring Au atoms, and organic ligands, and their intra- and inter-atomic interactions) to the relative stabilities of the four main AuNMs discussed in this work (see Figure 1a), supporting the thermal accessibility of the experimentally observed size-dependent transformations. Systematic DFT calculations of the initial 144-Au compound and the size-transformed products (i.e., TBBT-capped 133-Au, 191-Au, and 279-Au AuNMs) revealed the formation of delocalized electronic states, which, when analyzed with the use of the recently formulated (inner) core-cluster-shell model (CCSM), reveal electron fillings and shell closures following a superatom aufbau scheme, and opening of stabilizing HOMO-LUMO energy gaps for both the starting AuNM and each of the stable transformation product AuNMs recorded in the experiments.

To place the experimental strategy and the theoretical analysis described here in a broader context, it is pertinent to invoke here the concept of energy landscape, which has been developed earlier in the course of investigations of glass formation and the glass transition, and which has been employed and extensively developed in the context of investigations of protein conformations and protein folding.8 The analogy between the structural problem of relatively large organically capped metal clusters (e.g., composed of >100 Au atoms) and small protein molecules is rather close, regarding their molecular weight and the multitude and diversity of interactions characterizing their bonding modes and energetics, including covalent bonding and nonbonding interactions, i.e., a large number of dispersive (van der Waals) interactions. Additionally, the capped metal clusters exhibit metallic bonding including formation of superatom delocalized electronic shell orbitals, as well as metal-organic interactions. The essential characteristics of proteins being the dominant contribution of the very large number of distinct conformations and large number of weak interactions, thus requiring a statistical treatment which is the essence of the landscape picture. Consequently, it is sufficient for us to invoke here the picture of the potential energy surface (PES), which expresses the energy of a collection of atoms as a function of their coordinates (i.e., as a function of the geometry of that collection), with minima of the PES, occurring for certain values of the atomic coordinates, corresponding to energyfavorable structural configurations, with the deepest one being the optimal structure. The region of configuration space surrounding a local minimum of the PES, with the gradient of the energy as a function of the atomic coordinates pointing toward the minimum location, constitutes a basin of attraction. From a statistical mechanics point of view, the basin of attraction determines the probability of catchment of the

system at the configuration (structure) corresponding to the given energy minimum, or in its vicinity.

We thus use the PES picture for each size of the ligated metal clusters encountered in the course of the transformation reaction and regard the ligand-induced size structure transformation process as a chemical reaction guided by the properties of these PESs. Transitions between the various minima of the PES, entailing passage over encountered energy barriers separating the various local basins, were made possible by the elevated temperature maintained under the prevailing reflux conditions. This picture allows us to grasp the opportunity realized by the experimental protocol employed in this work, resulting in a unique comprehensive uninterrupted survey (bird's-eye view) of the size-evolutionary pattern of optimal gold nanomolecules in a broad size range (here, capped AuNMs with Au core sizes between 133 and 279 gold atoms). In particular, we note that the AuNMs (belonging to a TBBT-capped homologous sequence), identified here through measurements of analytes sampled along the temporal trajectory of the size-structure transformation reaction using mass spectrometry (MALDI-MS) and electron spray ionization (ESI-MS), have all been identified previously in separate experiments and their X-ray measured total structures have been determined. Interestingly, the inner cores of these AuNMs [see Figures 4 and 6-8] belong to a unique sequence that starts with the multitwinned 55-Au-atom icosahedral inner core for the capped Au<sub>133</sub> AuNM, <sup>16</sup> through the 89-Au-atom mono-twinned FCC D<sub>3h</sub> inner core of the "missing link" 191-Au-atom AuNM<sup>18</sup> (characterized by a limited catchment basin due to its unique structure and predicted to have marginal stability; see above), and culminating with the perfect FCC 147 Au-atom cuboctahedron inner core of the capped 279atom AuNM. 15 This observation suggests future use of the experimental methodology used in the current investigation in further studies. In particular, it would be of interest to repeat this experiment using a sufficiently different capping ligand, with the possibility of finding further optimal structures in this expanded size range.

We close by reiterating that the current work advances the methodology of structure and size transformation chemistry to sizes well beyond those reported in earlier studies. We indeed believe that the ability to induce structural and size transformation for AuNMs containing hundreds of atoms, demonstrated in this study, would provide the impetus for further research pertaining to the microscopic mechanisms that underlie and control these transformations, including the role of the ligands<sup>26,60</sup> (structure, functionality, bulkiness, interligand and ligand–metal interactions, electronic effects). We also trust that our findings would motivate future growth and application of nanomolecular metallurgy as an important methodology for the synthesis of new materials, as well as for fundamental studies in this exciting research area.

#### ASSOCIATED CONTENT

## Supporting Information

The Supporting Information is available free of charge at https://pubs.acs.org/doi/10.1021/acs.jpcc.1c04228.

MALDI-MS; ESI-MS; UV—vis absorption spectra; photon energy plot; crystal structures of  $\mathrm{Au}_{144}(\mathrm{SCH}_2\mathrm{Ph})_{60}$ ,  $\mathrm{Au}_{133}(\mathrm{SPh}\text{-}t\mathrm{Bu})_{52}$ ,  $\mathrm{Au}_{191}(\mathrm{SPh}\text{-}t\mathrm{Bu})_{66}$ , and  $\mathrm{Au}_{279}(\mathrm{SPh}\text{-}t\mathrm{Bu})_{84}$ ; computational details; and

electronic energies of various models and fragments (PDF)

## AUTHOR INFORMATION

#### **Corresponding Authors**

Alessandro Fortunelli — Consiglio Nazionale delle Ricerche, CNR-ICCOM, Pisa I-56124, Italy; o orcid.org/0000-0001-5337-4450; Email: alessandro.fortunelli@cnr.it

Uzi Landman — School of Physics, Georgia Institute of Technology, Atlanta, Georgia 30332, United States; orcid.org/0000-0002-1586-1554; Email: uzi@gatech.edu

Amala Dass — Department of Chemistry and Biochemistry, University of Mississippi, Oxford, Mississippi 38677, United States; occid.org/0000-0001-6942-5451; Email: amal@olemiss.edu

#### **Authors**

Kalpani Hirunika Wijesinghe — Department of Chemistry and Biochemistry, University of Mississippi, Oxford, Mississippi 38677, United States; occid.org/0000-0002-7049-0370

Naga Arjun Sakthivel — Department of Chemistry and Biochemistry, University of Mississippi, Oxford, Mississippi 38677, United States; Present Address: Waters Corporation, Taunton, Massachusetts 02780, United States; orcid.org/0000-0001-8134-905X

Luca Sementa – Consiglio Nazionale delle Ricerche, CNR-IPCF, Pisa I-56124, Italy

Bokwon Yoon — School of Physics, Georgia Institute of Technology, Atlanta, Georgia 30332, United States

Complete contact information is available at: https://pubs.acs.org/10.1021/acs.jpcc.1c04228

#### Note:

The authors declare no competing financial interest.

# ACKNOWLEDGMENTS

K.H.W., N.A.S., and A.D. gratefully acknowledge National Science Foundation Grant CHE-1808138, which supported this work. The work of U.L. and B.Y. was supported by grant FA9550-21-1-0198 from the U.S. Air Force Office of Scientific Research (AFOSR). Calculations and analysis of energetics were carried out at the Cineca Supercomputing Center within the ISCRA programme, which is gratefully acknowledged. The authors acknowledge useful conversations with Prof. R.L. Whetten about the early days of gold nanomolecules synthesis. Calculations of the electronic structure (Figures <sup>4</sup>–<sup>8</sup>) were carried out at the Georgia Institute of Technology Center for Computational Materials Science.

## REFERENCES

- (1) Whetten, R. L.; Khoury, J. T.; Alvarez, M. M.; Murthy, S.; Vezmar, I.; Wang, Z.; Stephens, P. W.; Cleveland, C. L.; Luedtke, W.; Landman, U. Nanocrystal Gold Molecules. *Adv. Mater.* **1996**, *8*, 428–433.
- (2) Hostetler, M. J.; Green, S. J.; Stokes, J. J.; Murray, R. W. Monolayers in Three Dimensions: Synthesis and Electrochemistry of ω-Functionalized Alkanethiolate-Stabilized Gold Cluster Compounds. *J. Am. Chem. Soc.* **1996**, *118*, 4212–4213.
- (3) Wey, K.; Epple, M. Ultrasmall Gold and Silver/Gold Nanoparticles (2 nm) as Autofluorescent Labels for Poly(D,L-

- lactide-co-glycolide) Nanoparticles (140 nm). J. Mater. Sci. Mater. Med. 2020, 31, No. 117.
- (4) Kawawaki, T.; Negishi, Y. Gold Nanoclusters as Electrocatalysts for Energy Conversion. *Nanomaterials* **2020**, *10*, 238.
- (5) Wu, Z.; Mullins, D. R.; Allard, L. F.; Zhang, Q.; Wang, L. CO Oxidation over Ceria Supported Au<sub>22</sub> Nanoclusters: Shape Effect of the Support. *Chin. Chem. Lett.* **2018**, *29*, 795–799.
- (6) Shen, H.; Xiang, S.; Xu, Z.; Liu, C.; Li, X.; Sun, C.; Lin, S.; Teo, B. K.; Zheng, N. Superatomic Au<sub>13</sub> Clusters Ligated by Different N-heterocyclic Carbenes and Their Ligand-Dependent Catalysis, Photoluminescence, and Proton Sensitivity. *Nano Res.* **2020**, *13*, 1908–1911.
- (7) Jadzinsky, P. D.; Calero, G.; Ackerson, C. J.; Bushnell, D. A.; Kornberg, R. D. Structure of a Thiol Monolayer-Protected Gold Nanoparticle at 1.1 Å Resolution. *Science* **2007**, *318*, 430–433.
- (8) Boisselier, E.; Astruc, D. Gold Nanoparticles in Nanomedicine: Preparations, Imaging, Diagnostics, Therapies and Toxicity. *Chem. Soc. Rev.* **2009**, 38, 1759–1782.
- (9) Brown, S. D.; Nativo, P.; Smith, J.-A.; Stirling, D.; Edwards, P. R.; Venugopal, B.; Flint, D. J.; Plumb, J. A.; Graham, D.; Wheate, N. J. Gold Nanoparticles for the Improved Anticancer Drug Delivery of the Active Component of Oxaliplatin. *J. Am. Chem. Soc.* **2010**, *132*, 4678–4684
- (10) Bunz, U. H.; Rotello, V. M. Gold Nanoparticle—Fluorophore Complexes: Sensitive and Discerning "Noses" for Biosystems Sensing. *Angew. Chem., Int. Ed.* **2010**, *49*, 3268–3279.
- (11) Favero, G.; Brugia, M.; Mancin, F.; Bonomi, R. Synthesis, Purification, and Characterization of Negatively Charged Gold Nanoparticles for Cation Sensing. *J. Chem. Educ.* **2019**, *96*, 2292–2290
- (12) Abbas, M. A.; Kamat, P. V.; Bang, J. H. Thiolated Gold Nanoclusters for Light Energy Conversion. ACS Energy Lett. 2018, 3, 840–854.
- (13) Zhao, S.; Austin, N.; Li, M.; Song, Y.; House, S. D.; Bernhard, S.; Yang, J. C.; Mpourmpakis, G.; Jin, R. Influence of Atomic-Level Morphology on Catalysis: The Case of Sphere and Rod-like Gold Nanoclusters for CO<sub>2</sub> Electroreduction. *ACS Catal.* **2018**, *8*, 4996–5001.
- (14) Du, Y.; Sheng, H.; Astruc, D.; Zhu, M. Atomically PreciseNnoble Metal Nanoclusters as Efficient Catalysts: A Bridge between Structure and Properties. *Chem. Rev.* **2020**, *120*, 526–622.
- (15) Sakthivel, N. A.; Theivendran, S.; Ganeshraj, V.; Oliver, A. G.; Dass, A. Crystal Structure of Faradaurate-279: Au279(SPh-tBu)84 Plasmonic Nanocrystal Molecules. *J. Am. Chem. Soc.* **2017**, 139, 15450–15459.
- (16) Dass, A.; Theivendran, S.; Nimmala, P. R.; Kumara, C.; Jupally, V. R.; Fortunelli, A.; Sementa, L.; Barcaro, G.; Zuo, X.; Noll, B. C. Au<sub>133</sub>(SPh-tBu)<sub>52</sub> nanomolecules: X-ray crystallography, optical, electrochemical, and theoretical analysis. *J. Am. Chem. Soc.* **2015**, 137, 4610–4613.
- (17) Yan, N.; Xia, N.; Liao, L.; Zhu, M.; Jin, F.; Jin, R.; Wu, Z. Unraveling the Long-Pursued Au<sub>144</sub> Structure by X-ray Crystallography. *Sci. Adv.* **2018**, *4*, No. eaat7259.
- (18) Sakthivel, N. A.; Shabaninezhad, M.; Sementa, L.; Yoon, B.; Stener, M.; Whetten, R. L.; Ramakrishna, G.; Fortunelli, A.; Landman, U.; Dass, A. The Missing Link: Au<sub>191</sub>(SPh-tBu)<sub>66</sub> Janus Nanoparticle with Molecular and Bulk-Metal-like Properties. *J. Am. Chem. Soc.* **2020**, *142*, 15799–15814.
- (19) Sakthivel, N. A.; Sementa, L.; Yoon, B.; Landman, U.; Fortunelli, A.; Dass, A. Isomeric Thiolate Monolayer Protected Au<sub>92</sub> and Au<sub>102</sub> Nanomolecules. *J. Phys. Chem. C* **2020**, *124*, 1655–1666.
- (20) Shibu, E.; Muhammed, M. H.; Tsukuda, T.; Pradeep, T. Ligand Exchange of Au<sub>25</sub>SG<sub>18</sub> Leading to Functionalized Gold Clusters: Spectroscopy, Kinetics, and Luminescence. *J. Phys. Chem. C* **2008**, *112*, 12168–12176.
- (21) Levi-Kalisman, Y.; Jadzinsky, P. D.; Kalisman, N.; Tsunoyama, H.; Tsukuda, T.; Bushnell, D. A.; Kornberg, R. D. Synthesis and Characterization of Au<sub>102</sub>(p-MBA)<sub>44</sub> Nanoparticles. *J. Am. Chem. Soc.* **2011**, 133, 2976–2982.

- (22) Negishi, Y.; Sakamoto, C.; Ohyama, T.; Tsukuda, T. Synthesis and the Origin of the Stability of Thiolate-Protected  $Au_{130}$  and  $Au_{187}$  Clusters. *J. Phys. Chem. Lett.* **2012**, *3*, 1624–1628.
- (23) Qian, H.; Eckenhoff, W. T.; Zhu, Y.; Pintauer, T.; Jin, R. Total Structure Determination of Thiolate-Protected Au<sub>38</sub> Nanoparticles. *J. Am. Chem. Soc.* **2010**, *132*, 8280–8281.
- (24) Qian, H.; Jin, R. Controlling Nanoparticles with Atomic Precision: The Case of Au<sub>144</sub>(SCH<sub>2</sub>CH<sub>2</sub>Ph)<sub>60</sub>. Nano Lett. **2009**, 9, 4083–4087.
- (25) Sakthivel, N. A.; Stener, M.; Sementa, L.; Fortunelli, A.; Ramakrishna, G.; Dass, A. Au<sub>279</sub>(SR)<sub>84</sub>: The Smallest Gold Thiolate Nanocrystal That Is Metallic and the Birth of Plasmon. *J. Phys. Chem. Lett.* **2018**, *9*, 1295–1300.
- (26) Rambukwella, M.; Sakthivel, N. A.; Delcamp, J. H.; Sementa, L.; Fortunelli, A.; Dass, A. Ligand Structure Determines Nanoparticles' Atomic Structure, Metal-Ligand Interface and Properties. *Front. Chem.* **2018**, *6*, 330.
- (27) Kurashige, W.; Niihori, Y.; Sharma, S.; Negishi, Y. Precise Synthesis, Functionalization and Application of Thiolate-Protected Gold Clusters. *Coord. Chem. Rev.* **2016**, 320–321, 238–250.
- (28) Tlahuice-Flores, A.; Whetten, R. L.; Jose-Yacaman, M. Ligand Effects on the Structure and the Electronic Optical Properties of Anionic Au<sub>25</sub>(SR)<sub>18</sub> Clusters. *J. Phys. Chem. C* **2013**, *117*, 20867–20875.
- (29) Pei, Y.; Gao, Y.; Zeng, X. C. Structural Prediction of Thiolate-Protected Au<sub>38</sub>: A Face-Fused Bi-Icosahedral Au Core. *J. Am. Chem. Soc.* **2008**, *130*, 7830–7832.
- (30) Nimmala, P. R.; Theivendran, S.; Barcaro, G.; Sementa, L.; Kumara, C.; Jupally, V. R.; Apra, E.; Stener, M.; Fortunelli, A.; Dass, A. Transformation of Au<sub>144</sub>(SCH<sub>2</sub>CH<sub>2</sub>Ph)<sub>60</sub> to Au<sub>133</sub>(SPh-tBu)<sub>52</sub> Nanomolecules: Theoretical and Experimental Study. *J. Phys. Chem. Lett.* **2015**, *6*, 2134–2139.
- (31) Zeng, C.; Liu, C.; Pei, Y.; Jin, R. Thiol Ligand-Induced Transformation of  $Au_{38}(SC_2H_4Ph)_{24}$  to  $Au_{36}(SPh-t-Bu)_{24}$ . ACS Nano **2013**, 7, 6138–6145.
- (32) Kang, X.; Zhu, M. Transformation of Atomically Precise Nanoclusters by Ligand-Exchange. *Chem. Mater.* **2019**, *31*, 9939–9969.
- (33) Eswaramoorthy, S. K.; Sakthivel, N. A.; Dass, A. Core Size Conversion of  $Au_{329}(SCH_2CH_2Ph)_{84}$  to  $Au_{279}(SPh-tBu)_{84}$  Nanomolecules. *J. Phys. Chem. C* **2019**, *123*, 9634–9639.
- (34) Chen, Y.; Liu, C.; Tang, Q.; Zeng, C.; Higaki, T.; Das, A.; Jiang, D.-e.; Rosi, N. L.; Jin, R. Isomerism in Au<sub>28</sub>(SR)<sub>20</sub> nanocluster and stable structures. *J. Am. Chem. Soc.* **2016**, *138*, 1482–1485.
- (35) Zeng, C.; Li, T.; Das, A.; Rosi, N. L.; Jin, R. Chiral Structure of Thiolate-Protected 28-Gold-Atom Nanocluster Determined by X-ray Crystallography. *J. Am. Chem. Soc.* **2013**, *135*, 10011–10013.
- (36) Zeng, C.; Qian, H.; Li, T.; Li, G.; Rosi, N. L.; Yoon, B.; Barnett, R. N.; Whetten, R. L.; Landman, U.; Jin, R. Total Structure and Electronic Properties of the Gold Nanocrystal Au<sub>36</sub>(SR)<sub>24</sub>. Angew. Chem., Int. Ed. **2012**, *51*, 13114–13118.
- (37) Zeng, C.; Liu, C.; Chen, Y.; Rosi, N. L.; Jin, R. Gold-Thiolate Ring as a Protecting Motif in the Au20(SR)16 Nanocluster and Implications. J. Am. Chem. Soc. 2014, 136, 11922-11925.
- (38) Nimmala, P. R.; Dass, A. Au<sub>99</sub>(SPh)<sub>42</sub> Nanomolecules: Aromatic Thiolate Ligand Induced Conversion of Au<sub>144</sub>(SCH<sub>2</sub>CH<sub>2</sub>Ph)<sub>60</sub>. J. Am. Chem. Soc. **2014**, 136, 17016–17023.
- (39) Dass, A.; Jones, T. C.; Theivendran, S.; Sementa, L.; Fortunelli, A. Core Size Interconversions of  $Au_{30}(S-tBu)_{18}$  and  $Au_{36}(SPhX)_{24}$ . *J. Phys. Chem. C* **2017**, *121*, 14914–14919.
- (40) Dainese, T.; Antonello, S.; Bogialli, S.; Fei, W.; Venzo, A.; Maran, F. Gold Fusion: From  $Au_{25}(SR)_{18}$  to  $Au_{38}(SR)_{24}$ , the Most Unexpected Transformation of a Very Stable Nanocluster. *ACS Nano* **2018**, *12*, 7057–7066.
- (41) Yao, Q.; Yuan, X.; Fung, V.; Yu, Y.; Leong, D. T.; Jiang, D.-e.; Xie, J. Understanding Seed-Mediated Growth of Gold Nanoclusters at Molecular Level. *Nat. Commun.* **2017**, *8*, No. 927.
- (42) Higaki, T.; Liu, C.; Chen, Y.; Zhao, S.; Zeng, C.; Jin, R.; Wang, S.; Rosi, N. L.; Jin, R. Oxidation-Induced Transformation of Eight-

- Electron Gold Nanoclusters:  $[Au_{23}(SR)_{16}]$  to  $[Au_{28}(SR)_{20}]^0$ . J. Phys. Chem. Lett. **2017**, 8, 866–870.
- (43) Wang, Y.; Nieto-Ortega, B.; Bürgi, T. Transformation from [Au<sub>25</sub>(SCH<sub>2</sub>CH<sub>2</sub>CH<sub>2</sub>CH<sub>3</sub>)<sub>18</sub>]<sup>0</sup> to Au <sub>28</sub>(SCH<sub>2</sub>CH(CH<sub>3</sub>)Ph)<sub>21</sub> Gold Nanoclusters: Gentle Conditions is Enough. *Chem. Commun.* **2019**, 55, 14914–14917.
- (44) Hesari, M.; Workentin, M. S. Facile Synthesis of Au<sub>23</sub>(SC-(CH<sub>3</sub>)<sub>3</sub>)<sub>16</sub> Clusters. *J. Mater. Chem. C* **2014**, *2*, 3631–3638.
- (45) Fihey, A.; Hettich, C.; Touzeau, J.; Maurel, F.; Perrier, A.; Köhler, C.; Aradi, B.; Frauenheim, T. SCC-DFTB Parameters for Simulating Hybrid Gold-Thiolates Compounds. *J. Comput. Chem.* **2015**, *36*, 2075–2087.
- (46) Martyna, G. J.; Klein, M. L.; Tuckerman, M. Nosé-Hoover Chains: The Canonical Ensemble via Continuous Dynamics. *J. Chem. Phys.* **1992**, *97*, 2635–2643.
- (47) Goedecker, S.; Teter, M.; Hutter, J. Separable Dual-Space Gaussian Pseudopotentials. *Phys. Rev. B: Condens. Matter Mater. Phys.* **1996**, *54*, 1703–1710.
- (48) VandeVondele, J.; Hutter, J. Gaussian Basis Sets for Accurate Calculations on Molecular Systems in Gas and Condensed Phases. *J. Chem. Phys.* **2007**, *127*, No. 114105.
- (49) Grimme, S.; Antony, J.; Ehrlich, S.; Krieg, H. A Consistent and Accurate Ab Initio Parametrization of Density Functional Dispersion Correction (DFT-D) for the 94 Elements H-Pu. *J. Chem. Phys.* **2010**, 132, No. 154104.
- (50) Perdew, J. P.; Burke, K.; Ernzerhof, M. Generalized Gradient Approximation Made Simple. *Phys. Rev. Lett.* **1996**, *77*, 3865–3868.
- (51) Kresse, G.; Hafner, J. Ab Initio Molecular Dynamics for Liquid Metals. *Phys. Rev. B: Condens. Matter Mater. Phys.* **1993**, 47, 558–561.
- (52) Kresse, G.; Hafner, J. Ab Initio Molecular-Dynamics Simulation of the Liquid-Metal—Amorphous-Semiconductor Transition in Germanium. *Phys. Rev. B: Condens. Matter Mater. Phys.* **1994**, 49, 14251–14269.
- (53) Kresse, G.; Furthmüller, J. Efficiency of Ab-Initio Total Energy Calculations for Metals and Semiconductors using a Plane-Wave Basis Set. *Comput. Mater. Sci.* **1996**, *6*, 15–50.
- (54) Kresse, G.; Joubert, D. From Ultrasoft Pseudopotentials to the Projector Augmented-Wave Method. *Phys. Rev. B: Condens. Matter Mater. Phys.* **1999**, *59*, 1758–1775.
- (55) Kresse, G.; Furthmüller, J. Efficient Iterative Schemes for Ab Initio Total-Energy Calculations using a Plane-Wave Basis Set. *Phys. Rev. B: Condens. Matter Mater. Phys.* **1996**, *54*, 11169–11186.
- (56) Perdew, J. P. Electronic Structure of Solids' 91. Akademie Verlag: Berlin, 1991.
- (57) Perdew, J. P.; Chevary, J. A.; Vosko, S. H.; Jackson, K. A.; Pederson, M. R.; Singh, D. J.; Fiolhais, C. Atoms, Molecules, Solids, and Surfaces: Applications of the Generalized Gradient Approximation for Exchange and Correlation. *Phys. Rev. B: Condens. Matter Mater. Phys.* 1992, 46, 6671–6687.
- (58) Perdew, J. P.; Chevary, J. A.; Vosko, S. H.; Jackson, K. A.; Pederson, M. R.; Singh, D. J.; Fiolhais, C. Erratum: Atoms, Molecules, Solids, and Surfaces: Applications of the Generalized Gradient Approximation for Exchange and Correlation. *Phys. Rev. B: Condens. Matter Mater. Phys.* 1993, 48, 4978.
- (59) Grimme, S. Semiempirical GGA-Type Density Functional Constructed with a Long-Range Dispersion Correction. *J. Comput. Chem.* **2006**, 27, 1787–1799.
- (60) Zeng, C.; Chen, Y.; Das, A.; Jin, R. Transformation Chemistry of Gold Nanoclusters: From One Stable Size to Another. *J. Phys. Chem. Lett.* **2015**, *6*, 2976–2986.
- (61) Koivisto, J.; Salorinne, K.; Mustalahti, S.; Lahtinen, T.; Malola, S.; Häkkinen, H.; Pettersson, M. Vibrational Perturbations and Ligand-Layer Coupling in a Single Crystal of Au144(SC2H4Ph)60 Nanocluster. *J. Phys. Chem. Lett.* **2014**, *5*, 387–392.
- (62) Lei, Z.; Li, J. J.; Wan, X. K.; Zhang, W. H.; Wang, Q. M. Isolation and Total Structure Determination of an All-Alkynyl-Protected Gold Nanocluster Au<sub>144</sub>. Angew. Chem. **2018**, 130, 8775–8779.

- (63) Elstner, M.; Porezag, D.; Jungnickel, G.; Elsner, J.; Haugk, M.; Frauenheim, T.; Suhai, S.; Seifert, G. Self-Consistent-Charge Density-Functional Tight-Binding Method for Simulations of Complex Materials Properties. *Phys. Rev. B* **1998**, *58*, 7260.
- (64) Hutter, J.; Iannuzzi, M.; Schiffmann, F.; VandeVondele, J. cp2k: Atomistic Simulations of Condensed Matter Systems. *Wiley Interdiscip. Rev.: Comput. Mol. Sci.* **2014**, *4*, 15–25.
- (65) Crasto, D.; Barcaro, G.; Stener, M.; Sementa, L.; Fortunelli, A.; Dass, A. Au<sub>24</sub>(SAdm)<sub>16</sub> nanomolecules: X-ray crystal structure, theoretical analysis, adaptability of adamantane ligands to form Au<sub>23</sub>(SAdm)<sub>16</sub> and Au<sub>25</sub>(SAdm)<sub>16</sub>, and its relation to Au<sub>25</sub>(SR)<sub>18</sub>. *J. Am. Chem. Soc.* **2014**, *136*, 14933–14940.
- (66) Yoon, B.; Koskinen, P.; Huber, B.; Kostko, O.; von Issendorff, B.; Häkkinen, H.; Moseler, M.; Landman, U. Size-Dependent Structural Evolution and Chemical Reactivity of Gold Clusters. *ChemPhysChem* **2007**, *8*, 157–161.
- (67) Knight, W.; Clemenger, K.; de Heer, W. A.; Saunders, W. A.; Chou, M.; Cohen, M. L. Electronic Shell Structure and Abundances of Sodium Clusters. *Phys. Rev. Lett.* **1984**, *52*, 2141–2143.
- (68) Walter, M.; Akola, J.; Lopez-Acevedo, O.; Jadzinsky, P. D.; Calero, G.; Ackerson, C. J.; Whetten, R. L.; Grönbeck, H.; Häkkinen, H. A Unified View of Ligand-Protected Gold Clusters as Superatom Complexes. *Proc. Natl. Acad. Sci. U.S.A.* **2008**, *105*, 9157–9162.
- (69) Desireddy, A.; Conn, B. E.; Guo, J.; Yoon, B.; Barnett, R. N.; Monahan, B. M.; Kirschbaum, K.; Griffith, W. P.; Whetten, R. L.; Landman, U.; et al. Ultrastable silver nanoparticles. *Nature* **2013**, *501*, 399–402.
- (70) Yannouleas, C.; Landman, U. Stabilized-Jellium Description of Neutral and Multiply Charged Fullerenes  $C_{60}^{x\pm}$ . Chem. Phys. Lett. **1994**, 217, 175–185.
- (71) Yannouleas, C.; Landman, U. Electronic Shell Effects in Triaxially Deformed Metal Clusters: A Systematic Interpretation of Experimental Observations. *Phys. Rev. B: Condens. Matter Mater. Phys.* 1995, 51, 1902.
- (72) Brust, M.; Walker, M.; Bethell, D.; Schiffrin, D. J.; Whyman, R. Synthesis of Thiol-derivatised Gold Nanoparticles in a Two-Phase Liquid-Liquid System. *J. Chem. Soc., Chem. Commun.* **1994**, *0*, 801–802
- (73) Colloidal Gold: Principles, Methods, and Applications; Hayat, M. A., Ed.; Academic Press: New York, 1989; Vols. 1–2.
- (74) Schaaff, T. G.; Whetten, R. L. Controlled etching of AuSR cluster compounds. J. Phys. Chem. B 1999, 103, 9394–9396.
- (75) Templeton, A. C.; Wuelfing, W. P.; Murray, R. W. Monolayer-Protected Cluster Molecules. *Acc. Chem. Res.* **2000**, 33, 27–36.
- (76) Whetten, R. L.; Khoury, J. T.; Alvarez, M. M.; Murthy, S.; Vezmar, I.; Wang, Z.; Cleveland, C. L.; Luedtke, W.; Landman, U. Nanocrystal Gold Molecules. In *The Chemical Physics of Fullerines 10 (and 3) Years Later*; Andreoni, W., Ed.; KluwerE. Applied Kluwer: Dordrecht, The Netherlands, 1996; pp 475–490.
- (77) Cleveland, C. L.; Landman, U. The energetics and structure of nickel clusters: Size dependence. *J. Chem. Phys.* **1991**, *94*, 7376–7396.
- (78) Nimmala, P. R.; Dass, A. Au36(SPh)23 Nanomolecules. J. Am. Chem. Soc. 2011, 133, 9175–9177.
- (79) Zeng, C.; Chen, Y.; Kirschbaum, K.; Appavoo, K.; Sfeir, M. Y.; Jin, R. Structural Patterns at all Scales in a Nonmetallic Chiral Au<sub>131</sub>(SR)<sub>52</sub> Nanoparticle. *Sci. Adv.* **2015**, *1*, No. e1500045.
- (80) Onuchic, J. N.; Shulten, L.; Wolynes, P. G. Theory of Protein folding: The energy landscape perspective. *Annu. Rev. Phys. Chem.* **1997**, *48*, 545–600.